Aus dem

Institut für Schlaganfall- und Demenzforschung (ISD)

Klinikum der Ludwig-Maximilians-Universität München

Designing and Monitoring DNA Origami Particles for Single-Cell Precision Delivery

Dissertation
zum Erwerb des Doctor of Philosophy (Ph.D.)
an der Medizinischen Fakultät der
Ludwig–Maximilians-Universität München

vorgelegt von
Müge Molbay

aus
Elazig/Türkei

Jahr
2024

Mit Genehmigung der Medizinischen Fakultät der
Ludwig-Maximilians-Universität München

Erstes Gutachten:	Prof. Dr. Nikolaus Plesnila
Zweites Gutachten:	Prof. Dr. Ali Ertürk
Drittes Gutachten:	Prof. Dr. Aloys Schepers
Viertes Gutachten:	Prof. Dr. Christian Plank

Dekan:	Prof. Dr. med. Thomas Gudermann

Tag der mündlichen Prüfung: 26.01.2024

The truest mentor in life is science.

Mustafa Kemal Atatürk

Table of content

Abstract:

Nanomedicine is a rapidly developing field that holds significant potential for targeted drug delivery and treatment of various diseases. Among the emerging technologies, DNA nanotechnology has gained attention for its versatility, biocompatibility, and programmability in constructing structures for targeted drug delivery. However, despite significant investments in these technologies, most are currently limited to *in vitro* evaluation. Moreover, the lack of tools for investigating the biodistribution of these structures at the cellular level hinders the ability to track them throughout the body. Recently, tissue-clearing methods have been developed to overcome these limitations and enable the exploration of intact biological specimens by rendering tissues transparent and imaging them using laser scanning fluorescence microscopy. Advancements in tissue clearing and light sheet microscopy have made it possible to investigate large volumes, such as whole mouse bodies, at cellular resolution. These new techniques provide a powerful tool for studying the biodistribution of DNA nanotechnology-based drug delivery systems *in vivo*, ultimately advancing the development of nanomedicine as a promising approach for treating a wide range of diseases.

In pursuit of developing an efficient and safe DNA nanotechnology-based drug delivery system, we generated DNA origami rods (8 nm x 80 nm) carrying fluorescent dyes. Prior to *in vivo* evaluation, we assessed the production efficiency and stability of the DNA origami *in vitro*, followed by evaluating its immune compatibility, half-life, targeting efficiency, and biodistribution in CD1 mice (n=5) after intravenous (iv) or oral administration. Results showed that the DNA origami treatment did not alter immune cell counts up to 7 days post-injection, indicating the immune safety of the treatment. *In vivo* imaging of the brain surface using intravital 2-photon microscopy revealed the clearance of the DNA origami from the meningeal blood circulation within 20 minutes post-injection, without any leakage into the brain parenchyma. In the periphery, the DNA origami was gradually cleared from the liver until 24 hours post-injection. Further, we investigated the biodistribution and targeting potential of DNA origami coupled with antibodies after iv injection. After 20 minutes of circulation, mouse bodies were subjected to vDISCO clearing and imaged using light sheet microscopy. Results showed that DNA origami coupled with CX3CR1 antibody was observable in lymph nodes, spleen, and Kupffer cells in the liver, while coupling with human carbonic anhydrase (CA) XII-specific antibody (6A10) directed the DNA origami to the lung where it co-localized with metastases in mice injected with MDA-MB-231 metastatic cancer cells. These findings demonstrate the potential of DNA origami-based drug delivery systems for targeted drug delivery, highlighting their potential for use in treating a range of diseases.

Thus, this approach can significantly help developing DNA nanotechnology for *in vivo* applications including drug delivery and gene editing. So far, our approach enables the assessment of biodistribution in the intact body with a sensitivity down to the single-cell level, revealing DNA origami's feasibility for drug targeting.

List of figures

List of tables

List of abbreviations

Abbreviations	Definition
3DISCO	3D imaging of solvent-cleared organs
6A10	Human carbonic anhydrase (CA) XII-specific antibody
AIF-1	Allograft inflammatory factor 1
ApoB1	Apolipoprotein B1
Apoe	Apolipoprotein E
BABB	benzyl alcohol and benzyl benzoate (1:2 vol:vol)
BBB	Blood-Brain Barrier
CA	Carbonic Anhydrase
CD11	Cluster of Differentiation Protein 11
CD16	Cluster of Differentiation Protein 16
CD3	Cluster of Differentiation Protein 3
CD32	Cluster of Differentiation Protein 32
CD45	Cluster of Differentiation Protein 45
CD69	Cluster of Differentiation Protein 69
CLARITY	Clear Lipid-exchanged Acrylamide-hybridized Rigid Imaging /Immunostaining / in situ-hybridization-compatible Tissue hYdrogel.
CUBIC	Clear, unobstructed brain/body imaging cocktails and computational analysis
CX3CR1	C-X3-C motif chemokine receptor 1
DMSO	Dimethyl sulfoxide
DNA	Deoxyribonucleic Acid
DOX	Doxorubicin
EDTA	Etheylenediaminetetraacetic acid
ER	Estrogen Receptor
FACS	Fluorescence-activated cell sorting
FITC	Fluorescein isothiocyanate
GFP/eGFP	Green Fluorescent Protein/enhanced Green Fluorescent Protein
HER2	Human Epidermal growth factor Receptor 2
iDISCO	Immunolabeling-enabled three-dimensional imaging of solvent-cleared organs
IFN-γ	Interferon Gamma
IgG	Immunoglobulin G
IL-12	Interleukin 12
iv	intravenous
kDa	kiloDalton
LDL	Low Density Lipoprotein
LSFM/ LSM	Light sheet Fluorescent Microscope/ Light sheet Microscope
MHCII	Major histocompatibility complex class II
MMF	Medetomidine, midazolam and fentanyl 11 mixture
mRNA	Messenger Ribonucleic Acid
NaCl	Sodium Chloride
NSG	NOD/SCID/IL2 receptor gamma chain knockout mouse line
PACT	Passive CLARITY Technique
PARS	Perfusion-assisted agent release in situ
PBS	Phosphate buffer saline

PDI	Polydispersity index
PEG	Polyethylene glycol
PEGPLys	Polyethylene glycol–poly(L)Lysine
PET	Positron emission tomography
PFA	Paraformaldehyde
PI	Propidium iodide
PR	Progesterone receptor
RI	Refractive Index
RNA	Ribonucleic Acid
ROI	Region of Interest
SDS-PAGE	Sodium dodecyl-sulfate polyacrylamide gel electrophoresis
SeeDB	See Deep Brain
SHIELD	Stabilization under harsh conditions via intramolecular epoxide linkages to prevent degradation
siRNA	Small interfering RNA
ssDNA	Single-stranded DNA
Sulfo-SMCC	Sulfosuccinimidyl 4-(N-maleimidomethyl) cyclohexane-1-carboxylate
TCEP	Tris(2-carboxyethyl)phosphine
TEM	Transmission Electron Microscope
THF	Tetrahydrofuran
TNBC	Triple-negative breast cancer
uDISCO	Ultimate 3D imaging of solvent-cleared organs
vDISCO	Nanobody(VHH)-boosted 3D imaging of solvent-cleared organs
VLDL	Very Low Density Lipoprotein

1. Introduction

1.1 Drug Design and Development

The process of drug design and development is a complex journey that requires a wide range of scientific expertise to ensure the quality, efficacy, and safety of the drug. This process can take up to fifteen years and involves pre-clinical research in cell-based and animal models, human clinical trials, and regulatory approval before the drug can be marketed (Figure 1).
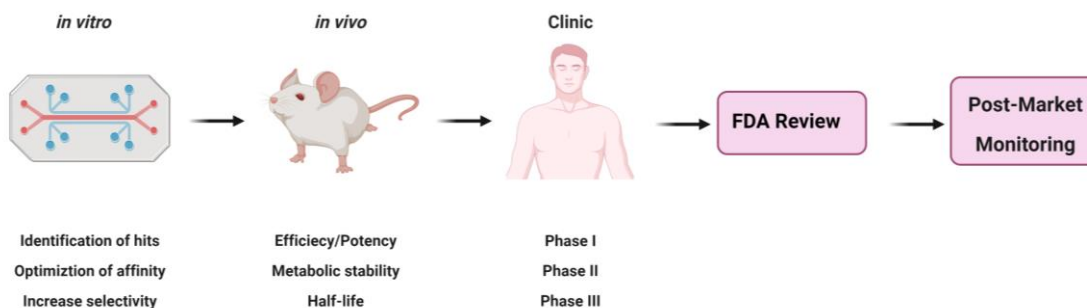
Figure 1: Schematic representation of the drug development process. Developing new drugs is a complex and intricate process that involves numerous stages, ranging from target identification and validation to clinical trials and regulatory approval. This schematic representation of the drug development process, created using BioRender.com, provides a clear overview of the sequential steps involved in this challenging endeavor.

Before clinical trials, several parameters need to be considered, including target identification and screening, optimization of targets to increase affinity and selectivity, efficacy/potency, metabolic stability, safety, toxicity, and immunogenicity, as well as oral bioavailability. Toxicological studies determine the maximum tolerated dose and effects of repeated dosing, while pharmacokinetic assays characterize how the drug is absorbed, distributed, metabolized, and excreted. Testing for carcinogenicity, immunotoxicity, drug-drug interactions, and other effects continues during clinical development. Early discovery activities have focused on evaluating the *in vitro* and *in vivo* potency of lead compounds and drug candidates. However, recent advances *in silico*, multi-omics, and biomarkers have improved the ability to predict the best targets with the highest selectivity (Muller and Milton, 2012).

In drug development, determining potency and efficacy is crucial for assessing pharmacodynamics and toxicological aspects. Potency is defined as the minimum amount of a drug necessary to elicit 50% of its maximal effect, while efficacy refers to the maximum effect that a drug can achieve. *In vitro* safety testing involves evaluating the potential off-target effects of a drug, carrier interactions, cytotoxicity, photo toxicity, and inhibition of cytochrome P450 enzymes, as well as conducting *ex vivo* experiments using isolated tissues. These tests provide critical information regarding the safety of a drug, which is essential for ensuring that it meets regulatory standards and can be approved for clinical use (Muller and Milton, 2012).

The concept of metabolic stability is essential due to its relation to metabolic clearance, which plays a crucial role in determining the bioavailability and half-life of a drug *in vivo*. Thus, it provides vital information about the dosage and frequency of administration of a drug. In nanoparticle production, optimizing metabolic stability is a significant challenge. If the particle is too stable, it may accumulate in the body, while if it is not stable enough, it may fail to reach the target site and achieve its intended function. Although *in vitro* models have shown limited success, current efforts have been directed towards developing computational models for predicting drug absorption, distribution, metabolism, and excretion parameters *in vitro* and/or *in vivo*. (Masimirembwa, Bredberg and Andersson, 2003).

Drugs are absorbed by the body and distributed to different tissues, including excretory organs like the liver and kidney, which can lead to a reduction in drug concentration in the blood or plasma. Clearance of drugs occurs mainly through two routes: renal and biliary excretion. For many compounds, hepatic clearance is a critical determinant of their overall pharmacokinetic properties, systemic elimination, and half-life. The liver contains numerous enzymes that produce less active metabolites upon the biotransformation of drugs. Drug metabolism refers to the conversion of fat-soluble chemicals into water-soluble forms for urinary excretion. The breakdown of drugs in the liver and their elimination through urine play a vital role in determining the drug's bioavailability, biosafety, and termination of drug and metabolite effects (Masimirembwa, Bredberg and Andersson, 2003).

The safety of a drug is determined by the occurrence of adverse drug reactions, which can manifest as either toxicity or immune reactions. During drug carrier and nanoparticle development, cell culture steps or chemical reactions may introduce endotoxins and toxic side products into the product. Toxicity arises when the liver or kidneys are unable to clear the drug from the bloodstream due to the presence of these side products or endotoxins, or when the dose exceeds the body's capacity to eliminate it, resulting in drug accumulation. Mechanism-based toxicity, immune hypersensitivity, off-target toxicity, and bio activation/covalent modification are the primary causes of drug toxicity. The most frequently observed incidences are related to cardiovascular and hepatic toxicity (Guengerich, 2011).

The successful development of a drug requires passing various stages of human/clinical trials. Hence, preclinical evaluations are vital to ensure selectivity, reduce the probability of undesirable side effects, and establish the drug's potency and efficacy. The optimization of metabolic stability is also crucial in extending the drug's half-life, increasing safety, and enhancing producibility and bioavailability while mitigating toxicity and immunogenicity risks.

1.2 DNA Nanotechnology

The DNA origami is a programmable and biocompatible platform that can combine different types, sizes, and numbers of molecules such as therapeutics, triggers, and imaging agents at the nanometer scale. The platform comprises various molecules including hydrophobic and hydrophilic ones, as well as organic and inorganic molecules, which can be assembled in a non-covalent or covalent manner. This allows to precisely controlling the dosage, the timing, and the location of the drug.

Nadrian Seeman laid the conceptual foundations of DNA nanotechnology in the early 1980s (Seeman, 1982). DNA nanotechnology involves the creation of synthetic DNA nanostructures through the manipulation of the physical and chemical properties of DNA, rather than its genetic properties (Arora and de Silva, 2018). This technique has numerous applications in biotechnology, and involves assembling long, single-stranded nucleic acid molecules into 2D and 3D nanostructures with sub-nanometer precision, using short oligonucleotides called "staples" (Figure 2) (Rothemund, 2006; Douglas *et al.*, 2009). DNA origami, a form of DNA nanotechnology, allows for the creation of self-assembled drug delivery structures using Watson-Crick base pairing. These structures can be combined with functional components such as small biomolecules, fluorescent dyes, metallic nanoparticles, peptides, proteins, or hydrophobic moieties, making them highly versatile (Czogalla et al., 2016; Simmel, 2012; Hong et al., 2017; Nummelin et al., 2018).
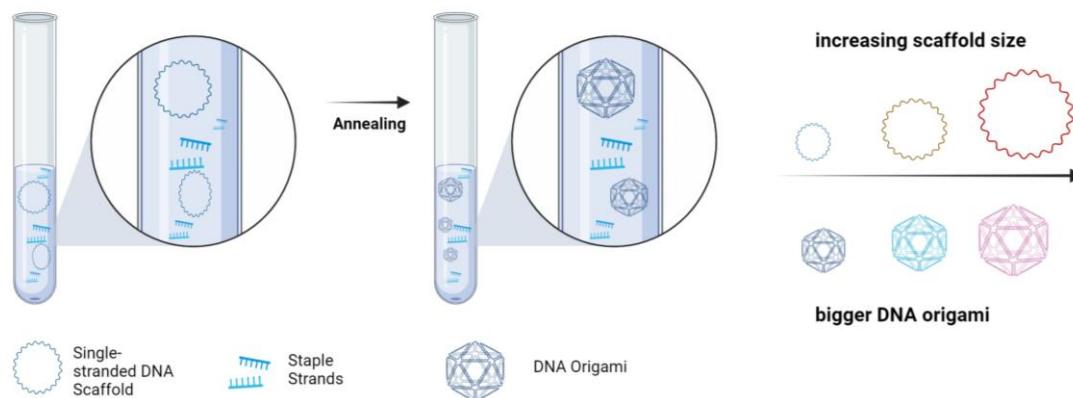
Figure 2: DNA origami nanoparticle assembly. DNA origami fold with a long single-stranded DNA scaffold and multiple staple strands via a thermal annealing process. Controlling the DNA origami size with custom scaffold lengths. Created with BioRender.com

1.2.1 Use of DNA Origami

DNA origami has become a promising tool in the field of nanotechnology due to its ability to produce predictable and programmable nanostructures. These structures have been used for various applications, including label-free RNA detection, charge release triggering, and immune stimulation (Chandrasekaran et al., 2016). Additionally, they have been utilized to deliver therapeutic modalities, such as drugs and gene-silencing constructs, while incorporating cellular targeting (Angell et al., 2016).

Recent advancements in DNA nanotechnology allowed for the programmed bottom-up assembly of designer nanostructures (Jones, Seeman and Mirkin, 2015; Xavier and Chandrasekaran, 2018) with wide-ranging applications in biosensing (Jones, Seeman and Mirkin, 2015; Chandrasekaran *et al.*, 2018), biomolecular analysis (Endo *et al.*, 2010a, 2010b), materials science (Sun *et al.*, 2014; Tian *et al.*, 2017), and molecular computation (Chandrasekaran *et al.*, 2017; Chandrasekaran, 2018). In particular, DNA origami is an extremely attractive strategy for self-assembled drug delivery structures as it enables the construction of predictable, programmable and fully organic nanostructures. By fabricating DNA nanostructures, researchers can achieve precise control over the size, shape, and spatial addressability of the resulting structures, while also allowing for high cargo capacity. This cargo can include therapeutic drugs, guided triggers, and imaging agents, which can be combined through covalent or non-covalent bonding to regulate drug dosage, timing, and localization (Rothemund, 2006). However, there are still challenges to be addressed, such as *in vivo* toxicity and addressability of DNA origami within the body.

1.2.2 *In vivo* Application of DNA Origami

A successful application of the DNA origami *in vivo* would require:
1) Mass production of origami structures that are stable and immune compatible,
2) Ability to target and track them with single-cell precision.
Despite its many advantages, multiple bottlenecks exist for the reliable and safe use of DNA origami *in vivo*. For example, immunogenicity created by DNA origami or its production method is one of the key questions to be addressed for effective *in vivo* use.

1.2.2.1 Mass production

The complexity and size of the assembled DNA origami nanostructures depend on the scaffold length, sequence, and production method used (Figure 2). One of the most cost-effective sources of single-stranded DNA (ssDNA) is the circular genome of the filamentous bacteriophage M13mp18, which is commercially available and contains 7,249 nucleotides in a circular form. This ssDNA can be easily utilized to assemble nanoparticles within the size range of 10 to 100 nm (Hong *et al.*, 2017). In 2006, Paul Rothemund utilized the higher replication rate of the engineered

M13 bacteriophage genome, known as M13mp18, to his advantage. This genome was engineered to Escherichia coli (E. coli), enabling the production of progeny phages without causing bacterial lysis, and the resulting phages were extracted to obtain purified ssDNA. As M13mp18 is circular, it has a higher replication rate than other sources of ssDNA (Rothemund, 2006), M13mp18 and a few of its length and sequence variants remain the primary sources of ssDNA scaffolds for DNA origami assembly (Yanisch-Perron, Vieira and Messing, 1985, p. 13; Douglas *et al.*, 2009; Nickels *et al.*, 2014).

New design software (Benson *et al.*, 2015; Jun, Shepherd, *et al.*, 2019; Jun, Zhang, *et al.*, 2019; Piskunen *et al.*, 2020) made the automated design of complex nanostructures possible, with any shape or size, and with an increasing number of biomedical applications (Chandrasekaran, 2016; Mathur and Medintz, 2019). These advancements have also led to the development of DNA nanoparticles with varying degrees of immune-compatibility through particular sequence designs (Surana, Shenoy and Krishnan, 2015). Eliminating undesirable effects, e.g. avoiding phage genes in the scaffold sequence or controlling the presence or absence of immunogenic CpG domains, is necessary for *in vivo* applications. Additionally, in order to enable a broader range of applications and reduce production costs, there is a need to significantly increase the scale of production of ssDNA scaffolds for biomedical applications.
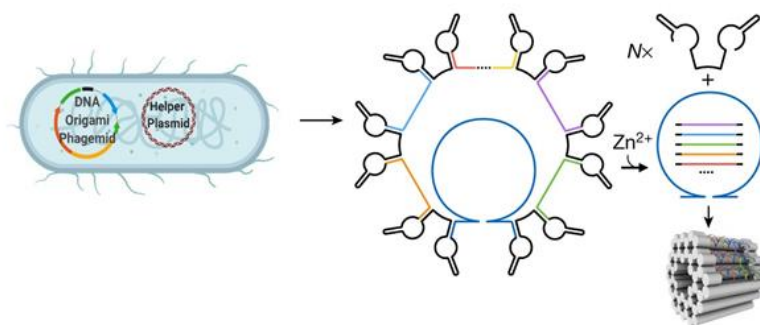
Figure 3: Schematic representation of phagemid ssDNA production: genes encoding M13 phage proteins are introduced either on a helper plasmid. Schematic representation of a single-stranded staple phagemid in which staples (colored) and scaffold (dark blue) are interleaved with DNAzyme sequences (black). Black ends of the staple strands indicate the constant overhangs that are generated by the DNAzymes (Praetorius *et al.*, 2017). Cleavage products can self-assemble into the target DNA origami.

Recent advances in biotechnology have opened new possibilities to produce ssDNA scaffolds for use in DNA origami design for biomedical applications. Praetorius et al. have developed a phagemid-based approach for the production of both the scaffold and staple ssDNA, which can be purified and used for one-pot assembly of DNA nanorods (Figure 3) (Praetorius *et al.*, 2017). Their study resulted in a total yield of 163 mg of folded DNA nanorods. In a similar approach, Engelhardt et al. have demonstrated a sequence design method that utilizes a split-ori phagemid to generate custom sequence-controlled scaffolds of various lengths that can be used to assemble 42 helix-bundles without CpG motifs (Engelhardt *et al.*, 2019). The avoidance of CpG motifs can reduce the CpG-induced immune response by avoiding Toll-like receptor-9-mediated immunogenic reactions, thus facilitating the *in vivo* use of DNA origami for biomedical applications (Krieg, 2002).

1.2.2.2   Enhancing Biostability and Extending Circulation Time

Nanoparticle-based drug delivery systems face the significant challenge of rapid and non-specific clearance *in vivo*. For good therapeutic efficacy, however, nanocarriers must have sufficient circulation time after intravenous administration (Wang *et al.*, 2013). DNA nanoparticles face additional challenges due to their biological nature. Firstly, they are susceptible to degradation by

deoxyribonucleases (DNases) in serum. Secondly, the ionic strength of body fluids is different from that of DNA assembly buffers, which may lead to the disassembly of DNA nanostructures at low cationic concentrations, due to increased electrostatic repulsion forces of negative DNA helices (Hahn *et al.*, 2014). Thirdly, non-specific adsorption of serum proteins can lead to an opsonization effect which triggers macrophages to engulf and clear DNA nanocarriers (Surana, Bhatia and Krishnan, 2013). Lastly, DNA nanostructures are highly prone to <u>fast renal or hepatic clearance</u> (Messaoudi, Greschner and Gauthier, 2019).

The stability of DNA structures can be improved by encapsulation. To this end, Shih et al. encapsulated DNA origami structures with liposomes and observed positive results in terms of enzyme protection and surface characterization (Figure 4) (Perrault and Shih, 2014a). In addition, cationic polymers, such as polyethylene glycol (PEG), can also be used for DNA structure encapsulation by binding to the negatively charged phosphate backbone of DNA via electrostatic interaction. However, the molecular ratio of polymers to DNA structures is critical, as improper ratios can lead to aggregation or degradation (Kiviaho *et al.*, 2016). Shih's group enveloped DNA barrels with oligolysine-PEG copolymers, which extended their blood half-life from 9 to 45 min and prevented rapid renal clearance (Ponnuswamy *et al.*, 2017). Inspired by spherical nucleic acids, Kim and Yin coated the outer surface of DNA brick nanostructures with dendritic oligonucleotides, which increased their biostability compared to their naked counterparts (Kim *et al.*, 2020). Finally, introducing thymidine-dimers into the scaffold strand using UV light can also increase stability by providing protection against DNases through the covalent bond between the dimer.
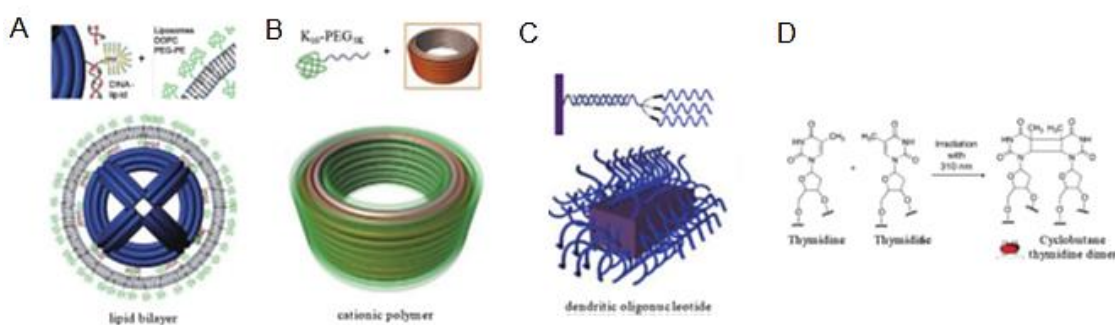
Figure 4: Improving the biostability and extending the circulation time of DNA nanocarriers are crucial steps for enhancing their therapeutic efficacy. To achieve this, several strategies have been developed, including lipid bilayer encapsulation of DNA nanocages (**A**), electrostatic coating of DNA origami nanostructures with polyamine-PEG block copolymers (**B**), dendritic oligonucleotides on DNA brick nanostructures (**C**), and light-triggered dimer formation of adjacent thymidine residues in DNA origami objects (**D**).

1.2.2.3   *In vivo* Distribution of Non-targeting DNA Origami

Several studies have investigated the biodistribution of DNA origami in various animal models. Generally, naked DNA nanostructures have accumulated mainly in the liver and kidneys. For instance, DNA tetrahedrons have been extensively studied as a straightforward DNA structure. To prevent liver accumulation, researchers have explored modifying the DNA backbone to increase biostability. Kim et al. reported that DNA tetrahedrons tend to accumulate in the liver after intravenous administration. They used this approach to reduce overexpression of ApoB1 in hypercholesterolemia by siRNA targeted to the liver thereby decreasing serum lipid levels by 20-30% compared to PBS controls (Kim *et al.*, 2016)(Kim *et al.*, 2020). In another study, Jiang et al. used positron emission tomography (PET) to study the biodistribution of radiolabeled DNA origami, and found that rectangle, triangle, and tube-shaped DNA origami were predominantly taken up by the kidneys (Jiang *et al.*, 2018). The small size (6-10 nm) and negative surface charge of DNA are advantageous for lymphatic drainage, and macrophages have been shown to easily take up DNA origami, providing good intracellular stability and extending their lymph node retention time. Additionally, Kim et al. labeled DNA tetrahedrons with a Cy5 fluorophore to visualize sentinel lymph nodes of tumors and showed enhanced translocation in lymph nodes and prolonged retention time in mice xenograft models (Kim *et al.*, 2013).

1.2.2.4   Targeting Strategies *in vivo*

Delivering DNA origami to specific organs or tissues of interest is a challenge after systemic administration. Achieving selective accumulation of drug molecules in targeted sites can enhance therapeutic efficacy and alleviate systemic toxicity associated with off-target delivery. Molecular ligands, such as antibodies, aptamers, receptor ligands, and functional peptides, can be conjugated onto DNA origami to achieve targeting functionality using various methods (Figure 5A) (Wu *et al.*, 2013; Setyawati, Kutty and Leong, 2016; Santi *et al.*, 2017). However, despite pronounced selectivity *in vitro*, some ligands cause a loss of targeting ability *in vivo* (e.g., transferrin) (Mirshafiee *et al.*, 2013). Despite exhibiting pronounced selectivity *in vitro*, some ligands, such as transferrin, lose their targeting ability *in vivo* due to complex biological content that inhibits molecular recognition capability and induces clearance by phagocytes when adsorbed by serum proteins (Oh *et al.*, 2018) (Figure 5B). Therefore, systematic studies and optimization are needed to improve *in vivo* delivery.
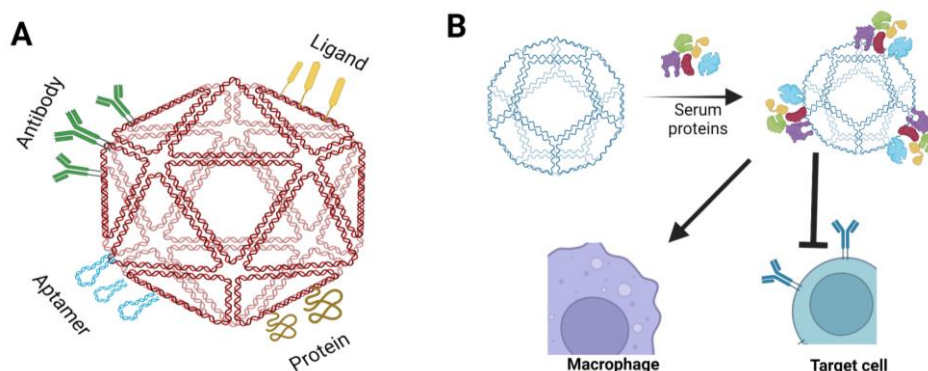
Figure 5: DNA nanocarriers targeting organs, tumors, and cells. (**A**) Modifications of DNA nanocarriers for active targeting to specific cells. (**B**) Non-specific protein adsorption to DNA nanocarriers in serum environment. Created with BioRender.com

Using DNA origami as a design tool can produce novel drugs and gene editing tools with high biocompatibility and high cellular uptake kinetics due to its production, stability, and targetability. Targeting immune or diseased cells allows the visualization of the delivery side and the treatment of many diseases.

1.3   Disease models for DNA Origami Application

1.3.1 Atherosclerosis

Atherosclerosis refers to a chronic inflammatory disease affecting large and medium-sized arteries, where fat, cholesterol, and other substances, accumulate as plaques within the artery wall and restrict blood flow. Chronic arterial inflammation is caused by prolonged exposure to oxidative stress factors and it involves multiple cell types and cellular mediators. Low-density lipoproteins contribute to the development and progression of atherosclerosis in two ways: firstly, oxidized lipids originating from low-density lipoproteins result in prolonged inflammation, and secondly, they cause the production of inflammatory cytokines. Diet and eating habits represent the main driving factors for the development of atherosclerosis, while genetic and epigenetic risk factors also have a significant impact (Linton *et al.*, 2000).

Commonly affected arteries include the aorta, carotid arteries, coronary arteries, and arteries of the lower extremities (Singh *et al.*, 2002). Rupture of atherosclerotic plaques in these arteries may trigger the formation of blood clots thereby causing heart disease and cerebrovascular accidents (Tulenko and Sumner, 2002; Nus and Mallat, 2016)(Hansson, 2005; Tuttolomondo *et al.*, 2012).

The Apoe$^{-/-}$ mouse model was generated using homologous recombination of embryonic stem cells and has been widely used in pre-clinical atherosclerosis studies (Zhang *et al.*, 1992). Apoe is a ligand responsible for the uptake of chylomicrons, very low-density lipoprotein (VLDL), and their remnants to hepatic receptors, such as LDL receptor and LDL receptor-related protein. The absence of the Apoe gene in these mice leads to impaired lipoprotein clearance, resulting in severe hypercholesterolemia, hyper- and dyslipoproteinemia, and the development of atherosclerotic lesions, even when fed a regular diet (von Holt *et al.*, 2009). Additionally, feeding these mice a high-fat or Western diet increases arterial fat deposition at earlier stages, making this model an appropriate tool to study atherosclerosis (Lo Sasso et al., 2016).

Proinflammatory phagocytic cells actively participate in the accumulation of cholesterol in growing atherosclerotic lesions (Figure 6). Studies in both mouse models and humans have linked CX3CR1 to atherosclerosis (Combadière *et al.*, 2003; Cybulsky and Hegele, 2003; Lesnik, Haskell and Charo, 2003; McDermott *et al.*, 2003; Bursill, Channon and Greaves, 2004; Teupser *et al.*, 2004; Apostolakis *et al.*, 2007). The fate of disease progression or regression is determined by different activation states of macrophages derived from inflammatory CX3CR1+ monocytes. CX3CR1 expressed in peripheral blood mononuclear cells can promote inflammation by facilitating leukocyte migration to the inflammatory lesion (Bjerkeli *et al.*, 2007). CX3CR1 is a promising target for developing anti-atherosclerotic therapies that could reduce monocyte recruitment to the lesion site, inhibit proinflammatory macrophages, or stimulate anti-inflammatory responses and cholesterol efflux.
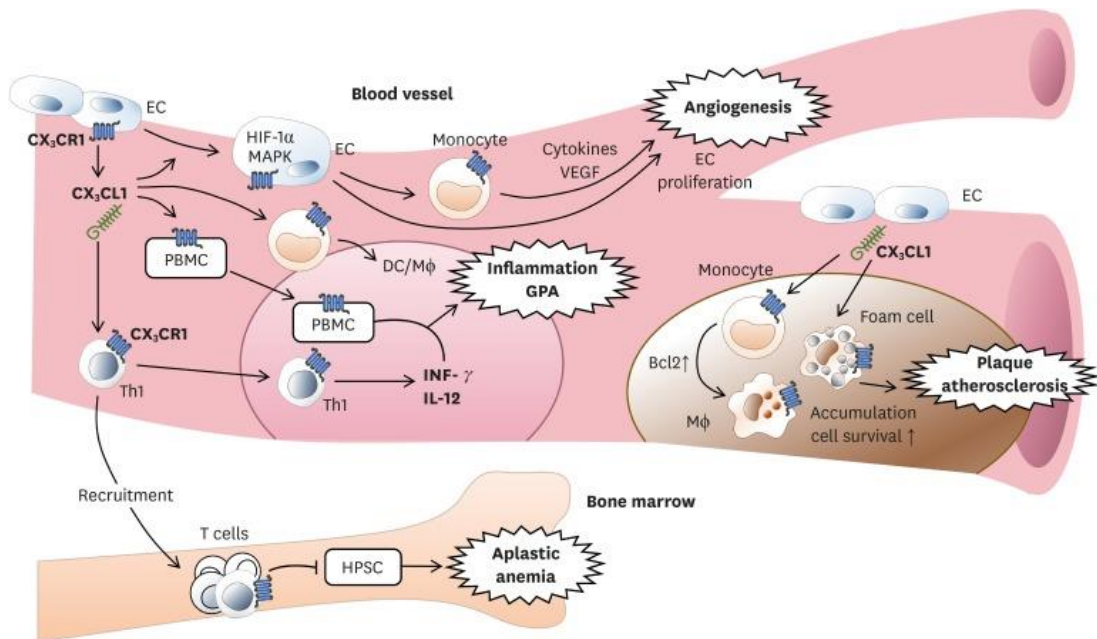
Figure 6: The role of CX3CR1+ cells in atherosclerosis progression. Activation of CX3CR1, expressed in peripheral blood mononuclear cells, causes leukocytes to migrate to the site of inflammation. CX3CR1-expressing Th1 also stimulates inflammation by secretion of IFN-γ and IL-12. For plaque, when CX3CL1 binds to CX3CR1 on monocyte, macrophage, and foam cells, these cells will accumulate in blood vessels and promote cell survival via expressing anti-apoptotic Bcl2 within cells (Lee *et al.*, 2018).

1.3.2 Breast Cancer

According to the World Health Organization, breast cancer is the most commonly occurring cancer in women and the second most common cancer overall, accounting for 11.7% of all cancer cases globally (Bray *et al.*, 2018). High metastasis rates are commonly associated with this disease, with approximately 90% of breast cancer-related deaths resulting from distal metastatic spreads rather than primary tumors (Lambert *et al.,* 2017). Consequently, breast cancer is widely

considered to be a systemic disease, requiring treatments that target both local and distal metastases (Redig and McAllister, 2013).

Breast cancer is commonly treated with standard chemotherapy or targeted therapy (Scully *et al.,* 2012). The former involves using cytotoxic chemicals that often lead to drug resistance and severe side effects (Alvarez, 2010). Targeted therapy primarily focuses on the estrogen receptor (ER), as seen with the use of tamoxifen (Nicolini *et al.,* 2006). A new therapeutic approach is immunotherapy using monoclonal antibodies that target specific cell surface receptors or enzymes (Nathan and Schmid, 2018). This innovative method has the potential to improve survival rates and reduce systemic side effects, making it an attractive treatment option for breast cancer patients.

Xenograft models have been developed to study human-specific drug targeting and altered gene function of breast cancer cell lines (Puchalapalli *et al.,* 2016). Carreno et al. introduced a new line of highly permissive human cancer metastasis engraftment called NOD-SCID-IL2 receptor γ null (NSG) (Carreno *et al.,* 2009). Subsequently, Iorns et al. reported that NSG mice allow the growth and metastasis of breast cancer cell lines from the orthotropic site (Iorns *et al.,* 2012) (Puchalapalli *et al.,* 2016). Therefore, NSG mice are frequently used for patient-derived xenograft models of breast cancer (Zhang and Lewis, 2013).

One widely used model in both *in vivo* and *in vitro* studies of breast cancer is the MDA-MB-231 cell line. This highly aggressive and invasive triple-negative breast cancer (TNBC) cell line lacks estrogen (ER) and progesterone receptors (PR) as well as HER2 amplification (Chavez, Garimella, and Lipkowitz, 2010). MDA-MB-231 cells are extensively studied and characterized in multiple aspects, including their molecular signature, metastasis profile, and response to various molecular drugs (Francia *et al.,* 2011).

Researchers have recently introduced a novel monoclonal antibody, 6A10, as a potential therapeutic agent against breast cancer metastasis. This antibody inhibits the function of carbonic anhydrases (CAs), which are overexpressed in various tumors, including breast cancer (Waheed, Sly and Doisy, 2017). Administering 6A10 to a mouse model of breast cancer metastasis (NSG) resulted in improved survival rates and reduced primary tumor signals, as observed through bioluminescence imaging (Gondi *et al.,* 2013). In combination with doxorubicin, 6A10 was able to eliminate nearly all lung metastases in experimental mice, whereas untreated controls or mice receiving only DOX showed little improvement (von Neubeck *et al.,* 2018). However, the limitations of bioluminescence imaging led to a subsequent study that utilized a deep learning-based algorithm, DeepMACT, to examine the efficiency of 6A10 in targeting whole-body metastasis. The results showed that the 6A10 antibody targeted 77% of metastasis, with the lung tissue being the primary site of metastasis (Pan *et al.,* 2019).

The tissue clearing technology allows all this advancement in monitoring and visualization of cancer treatment. Combined with deep learning, it provides an unbiased tool for cancer studies and many other diseases.

1.4 Tissue Clearing

Conducting intensive investigations of biological tissues is crucial to address fundamental biological questions. Nevertheless, current histological techniques face a variety of challenges, largely due to the diversity in sample size across different research questions. Slicing is a laborious process, and reconstructing three-dimensional views from adjacent slices is a time-intensive procedure that may result in the loss of critical information (Ertürk *et al.*, 2012). Consequently, rendering tissue transparent is a potential solution to overcome these difficulties while preserving tissue detail. Optical tissue clearing represents a broad term that encompasses various methods that rely on this concept. The approach of refractive index (RI) matching with the surrounding media has been widely adopted to achieve transparency, from the first tissue-clearing protocol to the latest methods available (Molbay *et al.*, 2021).

Werner Spalteholz is credited with describing the first tissue-clearing method in 1911. Spalteholz used a solution comprising of Methylsalicylate and Benzyl benzoate in a volume ratio of 5:3 to match the refractive index (RI) of the sample to the solution (Spalteholz, 1914). Embryologists adapted the Spalteholz method and substituted methyl salicylate with benzyl benzoate and benzyl alcohol to produce Murray's clear (BABB), which was a clear solution with a volume ratio of 1:2 for benzyl alcohol and benzyl benzoate (Dent, Polson and Klymkowsky, 1989; Klymkowsky and Hanken, 1991).

Tissue clearing is currently a powerful tool for obtaining single-cell resolution information within tissues, particularly with optical imaging and fluorescent labeling of cells. This has led to the development of various approaches, including hydrogel-based clearing, aqueous-based clearing, and solvent-based clearing using Spalteholz's historical recipe for tissue dehydration (Figure 7) (Silvestri *et al.*, 2016). Specialized protocols have been developed to expand the applications of tissue clearing for various purposes.

Hydrogel-based methods such as CLARITY (Chung *et al.*, 2013), PACT, and PARS (Yang et al., 2014) utilize an acrylamide monomer to form a tissue-hydrogel hybrid. This hybrid immobilizes most amino group-containing molecules by crosslinking, allowing large tissues to remain intact and reducing structural damage. The composition of the reagents can be modified depending on the intended imaging purpose, such as RNA or protein imaging. Additionally, tissue expansion is possible to enlarge and reveal potentially hidden structures. However, this approach requires longer incubation times for clearing and specialized equipment (Gradinaru *et al.*, 2018). Subtypes derived from this approach, such as PACT, PARS, SHIELD (Park *et al.*, 2019), and Bone CLARITY (Greenbaum *et al.*, 2017), are narrowly optimized for specific use cases. For instance, PACT is suitable for passive CLARITY, PARS is for whole-body clearing, and Bone CLARITY is a specialized protocol for investigating the compact and light-diffracting architecture of bone tissue. (Molbay *et al.*, 2021).
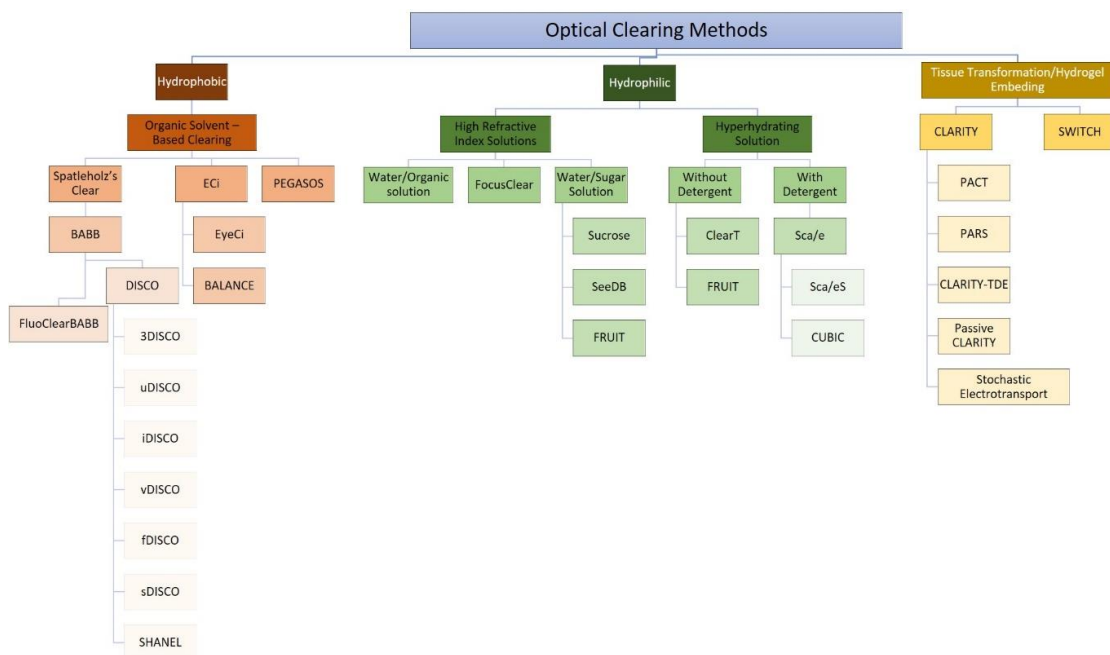
Figure 7: Grouping of most common tissue clearing methods. The various approaches for tissue clearing can be categorized into three main groups based on their chemical composition: hydrogel-based, hydrophilic, and hydrophobic. The subtypes within each group vary depending on the specific reagents and approaches used. Selection of the most appropriate method depends on several factors including the labeling method, tissue size, species, and the type of molecule of interest (Molbay *et al.*, 2021).

The second category of tissue clearing comprises hydrophilic or aqueous-based methods that were developed in the 1990s using various water-soluble agents such as sugars, dextran, sucrose, urea, and amino alcohols. Unlike hydrogel-based methods, these agents form hydrogen bonds with the tissue, making the approach less destructive and highly biocompatible and safe. The subtypes of hydrophilic methods differ based on the reagents used for decolorization, delipidation, and refractive index (RI) matching. i.e. urea in Sca/e (Hama *et al.*, 2011), urea with sorbitol in Sca/eS (Hama *et al.*, 2015), fructose for SeeDB (Ke, Fujimoto and Imai, 2013) and amino alcohols in CUBIC (Tainaka *et al.*, 2014).

On the other hand, hydrophobic or solvent-based methods, the descendants of Spalteholz's protocol, employ organic solvents to render tissues transparent. 3DISCO (3D imaging of solvent-cleared organs), which emerged from this method, can clear a whole mouse brain in one to two days, offering the advantages of fast and robust clearing (Ertürk *et al.*, 2012). The dehydration, delipidation, and RI matching steps are fundamental to this approach, with the dehydration step leading to tissue shrinkage in all DISCO methods except for iDISCO+ (Renier *et al.*, 2016). Nonetheless, this shrinkage has been beneficial in allowing for the imaging of an entire adult mouse body at cellular resolution using uDISCO (Pan *et al.*, 2016). By providing a systemic understanding of biology, this approach opens up new opportunities for reexamining biological questions and discoveries.

1.5   Research Aim

This thesis aims to examine the potential of DNA origami as a drug delivery system, however, DNA origami have not been investigated well *in vivo* so far. To fill this gap in DNA origami research, we combined tissue clearing, whole-body imaging, live imaging and molecular technique to examine stability, immune effects, targeting and biodistribution of DNA origami *in vivo*.

2. Material and Methods

2.1 DNA Origami Design and Production

The method to produce nanorod was adapted from the protocol described by Praetorius et al. (Praetorius *et al.*, 2017). The staple strands were arranged as a pseudogene, inter-leaved by self-excising DNAzyme cassettes. The pseudogene was then cloned into a phagemid backbone, which acted as a scaffold strand for the nanoparticles. The fully cloned phagemid was introduced into E. coli JM109 cells via transformation. Phage particles containing the phagemid single-stranded DNA were produced using helper phage rescue in a stirred-tank bioreactor. The phage and DNA were then purified to yield pure circular ssDNA. For the use *in vivo*, endotoxin was removed with Triton X 114, as described by Hahn (Hahn et al., 2014). Zinc cations were added to the purified ssDNA to activate the self-excising DNAzyme. This process yielded scaffold and staple strands for the nanorod. Following the DNA purification step with ethanol, the nanorod was assembled in a buffer containing 5 mM Tris, 5 mM NaCl, 1 mM EDTA, and 10 mM MgCl2 at a DNA concentration of 50 nM. The assembly was performed at 65°C for 15 minutes, followed by cooling to 60-45°C at a rate of 1°C per hour. For the vDISCO protocol, fluorescent-labeled DNA nanoparticle assembly was carried out using chemically synthesized single-stranded staple strands with Atto 550 or Atto 647N modification purchased from IDT or Biomers. The folding re-actions were set up as 100 µl or 2 mL reaction solutions, depending on the amount necessary for the *in vivo* experiments.
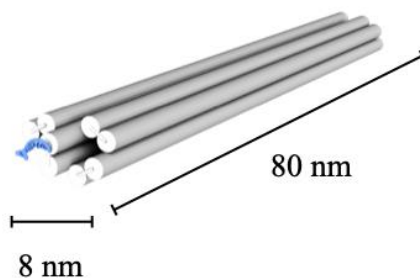
Figure 8: Shape and size of DNA origami nanorods used in the research.

2.2 DNA Nanorods Characterization

We successfully assembled DNA origami particles in a honeycomb organization to produce na-norods using single-stranded ~ 1000 nucleotide DNA oligonucleotide scaffolds and ~25 nucleo-tide single-stranded DNA staples. Our method, adapted from Praetorius et al. (Praetorius *et al.*, 2017), allows for the production of DNA origami structures by generating single-stranded oligo-nucleotides through excision from circular single-stranded DNA (ssDNA). The DNAzymes and the target oligonucleotides are part of the same DNA strand and are mass-produced together with the target DNA. The resulting DNA nanorod is 80 nm in length and 8 nm in dimension (Figure 13). Due to the negatively charged nature of the DNA molecule and its intermolecular repulsion forces, MgCl2 was used to neutralize it during the self-assembly of the DNA nanorod. However, during *in vivo* or *in vitro* applications, the removal or dilution of Mg2+ ions can lead to the denaturation and falling apart of the DNA origami structure. Our approach demonstrates the successful as-sembly of DNA origami particles into nanorods using a simple and efficient method. The use of single-stranded oligonucleotides generation allows for mass-production of the target DNA and DNAzymes, making it a cost-effective method. The resulting DNA nanorod has a precise dimen-sion and morphology, making it an attractive candidate for various biological applications. In con-clusion, our study displays the potential of using DNA origami particles in the design and fabrica-tion of nanorods. Further studies can explore the use of our method to produce DNA origami structures with different dimensions and shapes for various applications.
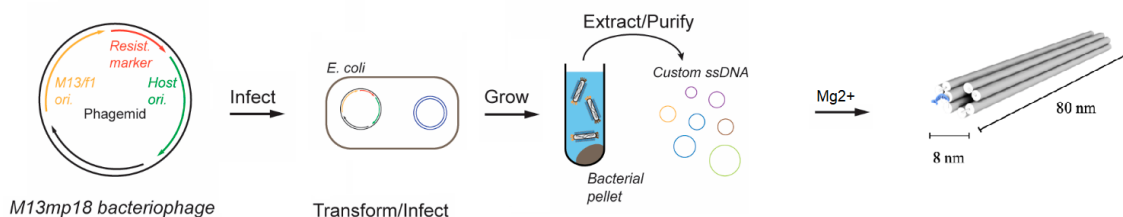
Figure 9: Schematic representation of DNA origami nanorod used in *in vivo* studies.

2.2.1 Preparation of IgG-ssDNA Conjugates

Oligonucleotides modified with 3' thiol modification were purchased HPLC purified and dried by Biomers. The oligos were dissolved in PBS (100 mM NaPi, 150 mM NaCl, pH 7.2) with 5 mM TCEP and incubated for 1h at RT. After three rounds of filter purification (10k Amicon Ultra 0-5 mL centrifugal filter), 10 nmol of the reduced thiol oligo was mixed with 10 equivalents of Sulfo-SMCC (sulfosuccinimidyl 4-(N-maleimidomethyl) cyclohexane-1-carboxylate, Thermo Scientific, dissolved in ddH2O) for 15 min. After three rounds of filter purification (10k Amicon Ultra 0-5 mL centrifugal filter), including buffer change to PBS (pH 8), 100 µg of antibody in PBS (pH 8) was added. The reaction was incubated for 4 h at 4°C at least. The conjugate was purified by ion-exchange chromatography (proFIRE, Dynamic Biosensors) using a NaCl gradient of 150-1000mM in PBS (pH 7.2). The purity of the oligo-antibody conjugates was analyzed by SDS-PAGE and agarose gel.
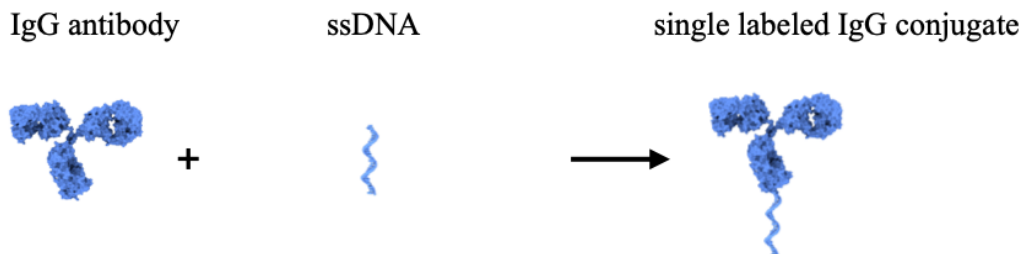
Figure 10: Oligonucleotide modification on IgG antibody for DNA origami coupling.

2.2.2 Assembly of Antibody Functionalized Nanorod

The nanorod equipped with up to four ssDNA strands complementary to the IgG-ssDNA conjugate was assembled and purified following the protocol of Stahl et al. with minor modifications (Stahl et al., 2014). The assembled nanorod was subjected to two rounds of PEG precipitation with PEG 8000 (8.25 % w/v) and NaCl (275 mM) at pH 8 to eliminate excess staple strands. The hybridization of IgG-ssDNA conjugate to the nanorod was accomplished in a buffer containing 5 mM Tris, 5 mM NaCl, 1 mM EDTA, and 10 mM MgCl2 at 30°C overnight. To concentrate the fully functionalized nanorod, a third round of PEG purification was performed followed by dissolving the nanorod in Tris buffer (5 mM Tris, 5 mM NaCl, 1 mM EDTA, and 5 mM MgCl2) at a high concentration of 4 µM. To ensure stability of the nanorod against low salt conditions and nuclease activity *in vivo*, we introduced PEG-polylysine (methoxy-poly(ethylene glycol)-block-poly(l-lysine hydrochloride), 10 lysine repeating units, 5 kDa MW PEG, Alamanda polymers) at an N:P ratio of 1:1. For *in vivo* experiments, we diluted the nanorod to 0.5 µM or 2 µM using sterile PBS to achieve a magnesium concentration of 2 mM or less. The endotoxin concentration of the fully equipped nanorod was determined using Endosafe Nexgen-PTS (Charles River) to comply with

23

the FDA's requirement of 36 EU/ml for a 100 µl interveinal injection per day (Malyala and Singh, 2008).
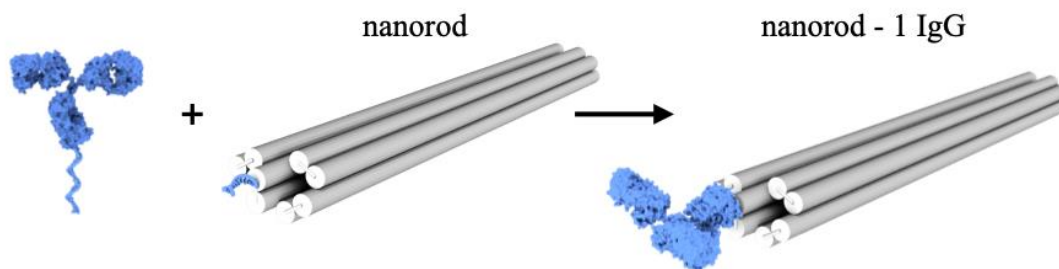
Figure 11: Coupling of antibody-oligonucleotide complex with DNA origami rods.

2.3 Animals

The mixed-gender CD-1 IGS mice (Charles River, stain code: 022), C57BL/6J (Jackson Laboratory, strain code: 000664), and female NSG (NOD/SCID/IL2 receptor gamma chain knockout) mice were procured from Charles River Laboratories and Jackson Laboratory. All animals were housed in the animal facility under a 12/12 hours light/dark cycle with access to food and water ad libitum. All animal experiments were approval by the Ethical Review Board of the Government of Upper Bavaria (Regierung von Oberbayern, Munich, Germany) and the Animal Experiments Council under the Danish Ministry of Environment and Food (2015-15-0201-00535) following the European directive 2010/63/EU for animal research. All data are reported according to the AR-RIVE criteria. Sample sizes were determined based on prior experience with similar models and are specified in the figure legends. Within each strain, animals were randomly selected for the experiments.

In accordance with the DeepMACT protocol (Pan et al., 2019a), MDA-MB-231 breast cancer cells expressing mCherry and enhanced-Firefly luciferase were counted, filtered, and resuspended in ice-cold DPBS at a concentration of 1×10^6 cells/mL. One hundred microliters of this cell suspension were injected in immune-deficient NSG mice. The growth of tumors was monitored by measuring bioluminescence (photons/second) of the whole body before DNA origami injection using an IVIS Lumina II Imaging System (Caliper Life Sciences). The mice were anesthetized with isoflurane, fixed in the imaging chamber, and imaged 15 minutes after luciferin injection (150 mg/kg; ip). The Living Image software 4.2 (Caliper) was used to quantify the bioluminescence signal. Two weeks after tumor cell injections, mice were randomly assigned to three different groups, i.e., the MgCl2 group, the DNA origami conjugated with eight Atto555 and a 6A10 antibody group, and the DNA origami conjugated with eight Atto555 group.

To establish an accelerated atherosclerosis model, Apolipoprotein E-deficient (apoE$^{-/-}$) mice were cross-bred with CX3CR1 fluorescent reporter mice (CX3CR1-eGFP). The resulting ApoE$^{-/-}$ CX3CR1-eGFP double transgenic mice were randomly assigned to groups and fed either a control or a high-fat (Western) diet for 4 weeks (early lesion group) or 16 weeks (advanced lesion group) to induce atherosclerotic lesions in the heart, aorta, and major arteries. Following the Western diet, animals were administered with immune-cell-targeting DNA origami with or without TMP195 conjugation, serving as a control for functional cargo delivery, and allowed to circulate for 20 minutes. Subsequently, the animals were sacrificed, perfused, and subjected to vDISCO.

2.4   Protein Corona and Zeta Potential of DNA Origami

The protein corona of nanoparticles was measured by Fluorescence Correlation Spectroscopy. DNA origami was dissolved in HEPES buffer or serum-containing media with various concentrations (70%, 90%, and 99%). The folded capillary cell containing the samples was then measured three times, with six sub-runs each, at a temperature of 25°C.

2.5   Immunotoxicity Assessments

In this study, we investigated the effects of naked DNA origami injection on immune cells in mixed-gender CD-1 mice. Tail-vein injections of naked DNA origami were administered at a concentration of 2 μM x 100 μl for each mouse (n=5), with and without purification, and blood and spleen samples were collected after 4h and 24h. Gavage injections of DNA origami were also administered at a concentration of 2μM x 400μl for each mouse (50.725 mg/kg per animal; n=5), and blood samples and spleens were collected after 4h and 24h. Flow cytometry analysis was performed to investigate the activation of immune cells. To examine the effects of DNA origami injection, body weight, body temperature, and neurological function was assessed on days 1, 3, 5, and 7 after injection. Flow cytometry analysis was performed in the same way for both experiments. Erythrocytes were lysed using isotonic ammonium chloride buffer, and after cardiac puncture, mice were perfused with normal saline for dissection of the spleen. Spleens were transferred to tubes containing Hank's balanced salt solution (HBSS), homogenized, and filtered through 40 μm cell strainers to obtain single-cell suspensions. To isolate leukocytes from homogenized spleens, erythrolysis was performed using an isotonic ammonium chloride buffer. To characterize the surface markers of different cell types, including CD45+ leukocytes, CD45+CD11b+ monocytes (+ MHCII+ expression), CD3+ T cells, and CD3+CD69+ activated T cells, we used anti-mouse antibodies and performed Fc blocking (Anti CD16/CD32, Invitrogen) on all samples prior to extracellular antibody staining. All staining procedures were conducted following the manufacturer's protocols. Flow cytometric data was acquired using a BD FACSverse flow cytometer (BD Biosciences) and analyzed using FlowJo software (Treestar). The animal experiments were conducted according to the institutional guidelines set forth by the Klinikum der Universität München / Ludwig Maximilian University of Munich, and after approval of the Ethical Review Board of the Government of Upper Bavaria (Regierung von Oberbayern, Munich, Germany) and the Animal Experiments Council under the Danish Ministry of Environment and Food (2015-15-0201-00535) in accordance with the European directive 2010/63/EU for animal research.
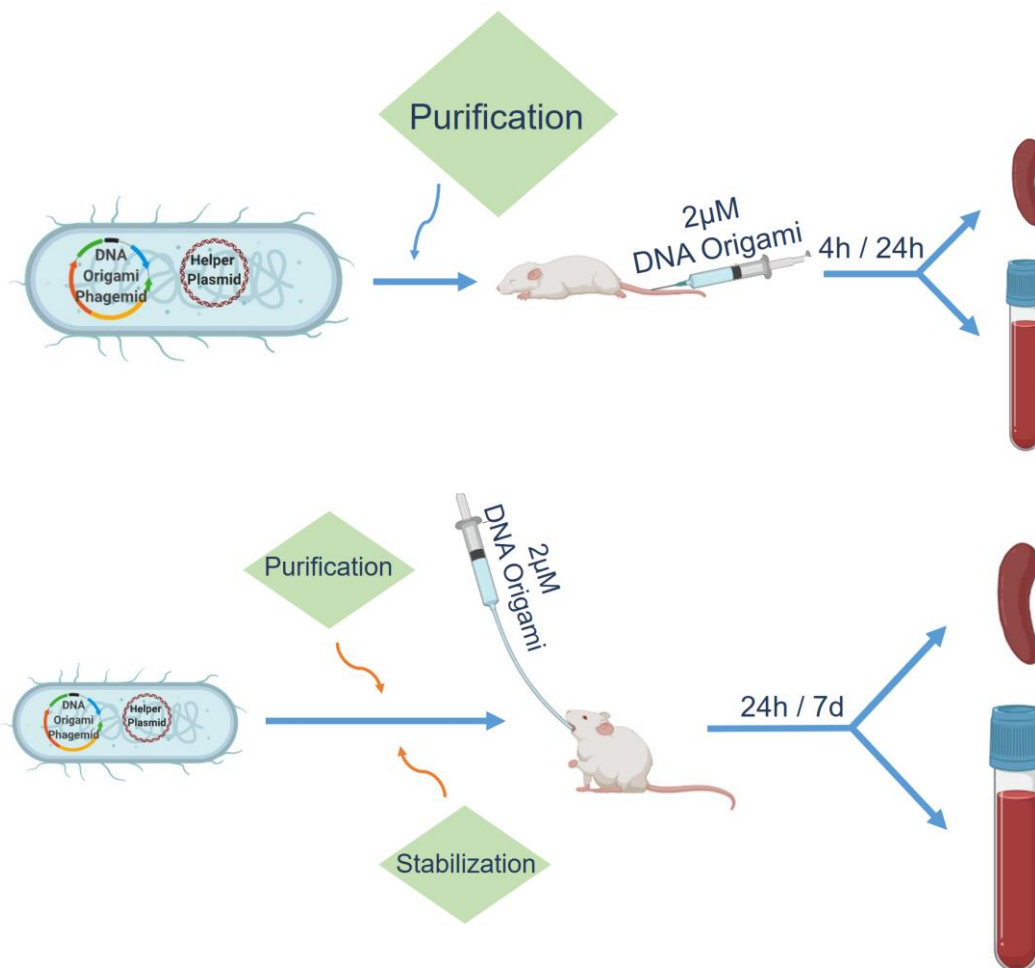
Figure 12: Schematics of immune reaction assessments against DNA origami. After producing origami rods in E.coli, particles are purified from endotoxin impurities. For acute phases, 100 µL of 2 µM unconjugated origami was injected through the tail vein and after 4 hours or 24 hours blood and liver samples were collected. For acute phase assessments and to test oral administration, 400 µL of 2 µM unconjugated, PEG-PLys origami was administrated through gavage. After 24 hours or 7 days, blood and liver samples were collected.

2.6   Non-targeting DNA Origami Half-Life in Blood

In vivo 2-photon imaging was used to investigate the half-life of non-targeting DNA origami in blood. An upright confocal microscope (Zeiss MP7) equipped with a Ti:Sa laser (Chameleon Vision II, Coherent) and two fluorescence detectors for red and green light were used for imaging. All animal experiments were performed according to institutional guidelines and approved by the Government of Upper Bavaria. 8-week-old C57BL/6N mice were obtained from Charles River Laboratories and anesthetized intraperitoneally (ip) with a combination of medetomidine (0.5 mg/kg), fentanyl 11 (0.05 mg/kg), and midazolam (5 mg/kg) (MMF). Body temperature was monitored and maintained using a rectal probe attached to a feedback-controlled heating pad throughout the experiment. A catheter was placed in the femoral artery to administer the fluorescent dye or nanoparticles. A rectangular 4x4-mm cranial window was drilled over the right frontoparietal cortex under continuous cooling with saline to identify the brain vessels and obtain a baseline image, as described previously (Khalin et al., 2020). The mouse was injected with FITC-dextran 3 µL/g before being placed on the multiphoton microscope adapted for intravital imaging of small animals. Non-targeting DNA origami, conjugated with Atto-550, was injected at a concentration of 1 µM and a dose of 120 µL. We performed scanning using time series, with an 80 µm depth and a laser power of 10% at 800 nm wavelength, utilizing a GAASP detector with an LP < 570

nm filter and a master gain of 600 for the FITC channel, and LP > 570 nm for the NPs channel with a master gain of 600. The total imaging time did not exceed 70 minutes. FIJI software was used for fluorescence analysis.

2.7 Biodistribution and Clearance of DNA Origami

Polyethylene tubing with an inner diameter of 0.28 mm and outer diameter of 0.61 mm was heated and pulled to obtain a cone-shaped tip. The catheter tips were carefully examined under a stereomicroscope (magnification, 31.5x; SZX 10, Olympus). Capillaries were flushed with sterile 0.9% NaCl before use. CX3CR1GFP-/+ mice were anesthetized with 5% isoflurane (Forene, Abbott) in oxygen (300 mL/min) and placed on a heating pad (Horn) to maintain body temperature at 37°C. Throughout the surgical procedure, anesthesia was maintained using an inspiratory isoflurane concentration of 2%. The surgical procedure was performed under a stereomicroscope. A skin incision of 3 to 4 mm parallel and inferior to the inguinal ligament was made to expose the left femoral artery, vein, and nerve. The femoral vein was separated from the surrounding tissues, and the capillary was replaced with polyethylene tubing by advancing the thinned tip into the artery. Subsequently, 100 µl of different solutions (MgCl2 buffer, Atto647- PEGPLys, DNA origami- Atto647- PEGPLys (0.5 µM), and goat anti-mouse CX3CR1 antibody conjugated DNA origami (0.5 µM) were injected through the capillary (Figure 12). Animals were sacrificed 20 minutes, 4 hours, or 24 hours after injection.
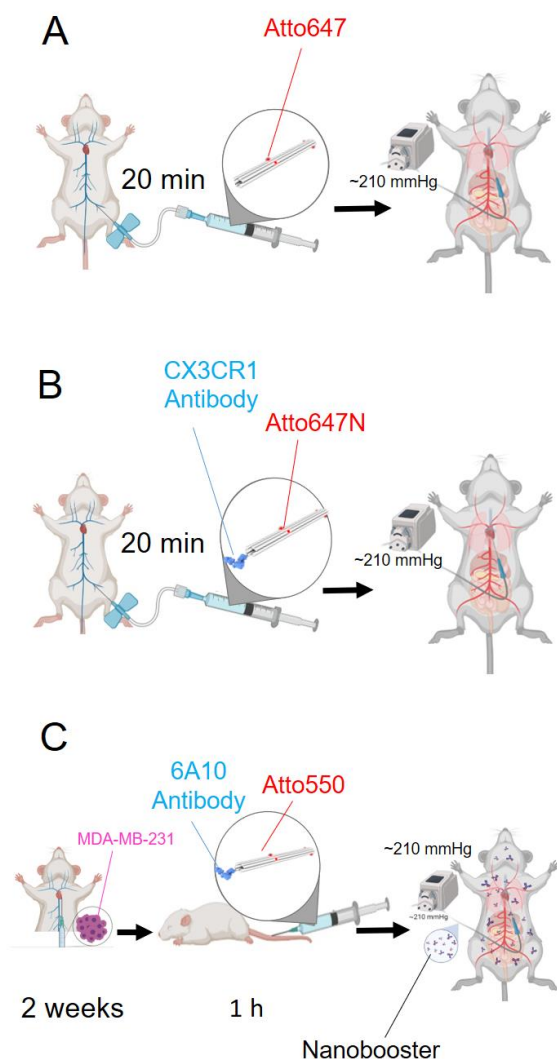

Figure 13: Schematics of biodistribution assessments of different origami moieties.

2.8   Therapeutic Targeting of Functional Cargo with DNA Origami

Two weeks after tumor cell injections, mice were randomly assigned to three different groups, i.e., the MgCl2 group, the DNA origami conjugated with eight Atto555 and a 6A10 antibody group, and the DNA origami conjugated with eight Atto555 group. The substances were administered through the tail vein and allowed to circulate for one hour before perfusion (Figure 12). To be able to evaluate the cargo capability of DNA origami, we conjugated it with Doxorubicin (DOX) (Figure 14), a potent anticancer medication and injected it through tail-vein. We used DOX as control, after 6h we perfused and vDISCO cleared the whole bodies. Moreover, we utilized DeepMACT quantification, an unbiased method, to evaluate the effects of DNA origami-DOX conjugates on cancer metastasis based on previously published algorithm (Pan et al., 2019a).

After the induction of atherosclerosis with high fat diet, animals received goat anti-mouse CX3CR1 antibody conjugated DNA origami (0.5 µM) through tail vein and after 20 minutes, they were sacrificed and subjected to vDISCO and analyzed for macrophage targeting in the atherosclerotic lesion. Another atherosclerotic macrophage targeting DNA origami has been designed to carry functional cargo of TMP195 (Figure 14) to inhibit protein expression and to provide a selective immunesuppression at the atherosclerotic site.
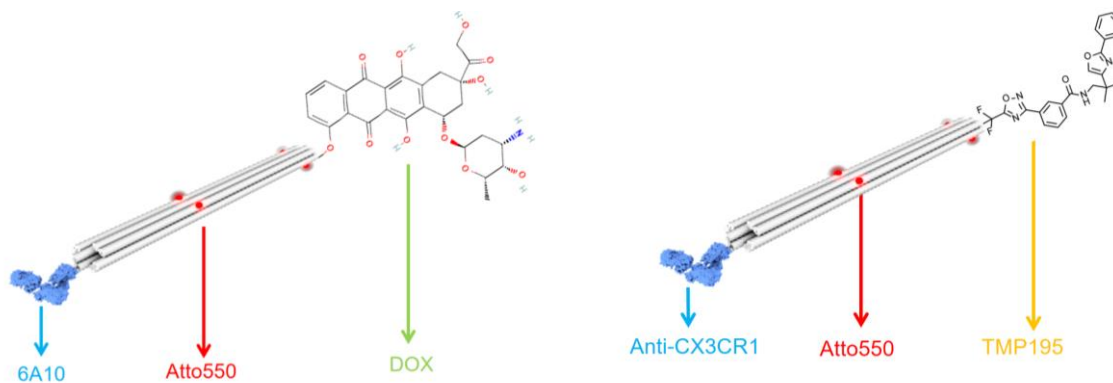
Figure 144: Schematics of functional cargo conjugated different origami moieties. DOX is a small chemotherapeutic drug, inhibiting topoisomerase II disrupts DNA repair and cell growth. TMP 195 is a Histone Deacetylase 9 (HDAC9) inhibitor, that prevent the protein expression and eventually induce apoptosis.

2.9   Whole-body Clearing

Whole-body clearing of CX3CR1 mice was performed using the vDISCO protocol (Cai et al., 2019). Decalcification solutions and decolorization solutions were perfused to remove the opacity of residual blood and bones before staining. Decolorization solution was prepared with a 25 vol% dilution of CUBIC reagent (25 wt% urea, 25 wt% N,N,N′,N′-tetrakis (2-hydroxypropyl)ethylenedi-amine, and 15 wt% Triton X-100) in 0.01 M PBS. The decalcification solution was 10 wt/vol% EDTA with pH 8. All solutions were applied by transcardiac injections through the same route used for PBS and PFA perfusion. The mouse was placed in a 300 ml glass chamber, filled with 250-300 ml of the appropriate solution, and the transcardial circulatory system was established with a peristaltic pump, keeping the pressure at 160-230 mmHg. The needle tip was fixed in place with superglue to ensure extensive perfusion. After post-fixation and PBS washing, mice were first perfused with 0.1 M PBS overnight at room temperature, followed by perfusion with 250 ml of decolorization solution for 2 days. Mice were then perfused with 0.01 M PBS and washed three times for 3 hours followed by perfusion with 250 ml of decalcification solution for 2 days at room temperature, and again perfusion/washing with 0.01 M PBS three times for 3 hours. Next, the

mice were incubated in permeabilization solution (1.5% goat serum, 0.5% Triton X-100, 0.5 mM of methyl-β-cyclodextrin, 0.2% trans-1-acetyl-4-hydroxy-l-proline, and 0.05% sodium azide in 0.01 M PBS). Subsequently, mice were perfused for 6 days with 250 ml of the same permeabilization solution containing 290 µl of PI (stock concentration 1 mg ml−1) and 35 µl of nanobody (stock concentration 0.5-1 mg/ml) for cancer-bearing animals to boost mCherry signal. The mice were washed out by perfusing with 0.01 M PBS three times for 3 hours at room temperature. After staining, the mice were cleared using a 3DISCO-based passive whole-body clearing protocol optimized for large samples. Mice were placed in glass chambers on top of a shaking rocker (IKA, 2D digital). They were subjected to THF series in different concentrations for dehydration; 50 vol% THF, 70 vol% THF, 80 vol% THF, 100 vol% THF and again 100 vol% THF, (12 h for each step). Finally, mice were subjected to dichloromethane 3h and in BABB. The glass chamber was sealed with parafilm and covered with aluminum foil during all incubation steps.

To examine the co-localization of CX3CR1 antibody conjugated DNA origami-Atto with CX3CR1 positive immune cells, such as monocytes, B cells, T cells, and macrophages, liver samples were rehydrated as follows: first with dichloromethane (DCM), then with 100%, 70%, and 50% THF, and finally with PBS for two cycles. The rehydrated livers were sliced into 1mm thick sections using a vibratome (Leica, VT1200S) for immunostaining. The sections were blocked with a blocking buffer consisting of 10% goat serum, 10% dimethyl sulfoxide (DMSO) (Roth, A994.2), and 0.2% Triton X-100 in PBS at room temperature for 2-3 hours. Next, the sections were incubated with a primary antibody solution containing rabbit antibody anti-CX3CR1 (1:1000, 14-6093-81, Abcam) and CD68 (1:1000, Ab125212, Abcam) in a buffer of 10mg·L-1 heparin, 3% goat serum, 0.2% Tween-20, 3% DMSO in PBS for 2 hours at 37°C. After washing with a washing buffer containing 0.2% Tween-20 and 10mg·L-1 heparin in PBS three times, Alexa 647-conjugated secondary antibodies (1:500, Thermo Fisher) were added to the sample in the same buffer as the primary antibody. The samples were washed with PBS and then imaged using a Zeiss LSM 880 confocal microscope equipped with a 40x oil-immersion objective (Zeiss, ECPlan-NeoFluar 40x, NA 1.30) for higher magnification. To maintain tissue transparency, the cleared samples were placed on the glass bottom of MatTek Petri dishes (35 mm) and immersed in several drops of BABB solution. Zen 2 software (v.10.0.4.910; Carl Zeiss AG) was used to analyze all images.

2.10 Light-sheet Microscopy Imaging

Image acquisition was performed using an ultramicroscope (LaVision BioTec) for single-plane illumination (light-sheet) with a 4 µm axial resolution. The following filter sets were used: ex. 470/40 nm, em. 535/50 nm; ex. 545/25 nm, em. 605/70 nm; ex. 560/30 nm, em. 609/54 nm; ex. 580/25 nm, em. 625/30 nm; ex. 640/40 nm, em. 690/50 nm. For whole-body imaging of the Cx3Cr1-eGFP mouse at low magnification, we utilized a 1x Olympus air objective (Olympus MV PLAPO 1x/0.25 NA [WD = 65mm]) coupled to an Olympus MVX10 zoom body, which provided zoom ranging from 0.63x to 6.3x. We acquired a 2 × 2.5 cm field of view using a 1x objective and 0.63x of zoom, covering the entire width of the mouse body. Tile scans were obtained from the ventral and dorsal surfaces up to 12 mm in depth, with a 40% overlap along the longitudinal y-axis of the mouse body, and a z-step of 8 µm. The exposure time was 120 ms, the laser power was adjusted based on the fluorescent signal intensity, and the light-sheet width was kept at maximum. After tile imaging, scanned regions were removed using a thin motorized dental blade (0.2 mm) (Dremel 8200) for further imaging. After whole-body imaging, we imaged the lungs, liver, and spleen of CX3CR1-eGFP animals injected with MgCl2 buffer, Atto647-PEG, DNA origami-Atto647-PEG (0.5 µM), or goat anti-mouse CX3CR1 antibody-conjugated DNA origami (0.5 µM) using a 12x objective (Olympus MVPLAPO2XC/0.5 NA [WD = 6 mm]).

2.11 Confocal Microscopy Imaging

Sample preparation is a crucial step for imaging thick cleared specimens, such as dissected tissues, pieces of organs, or whole organs. The specimens were placed on 35 mm glass-bottom Petri dishes (MatTek, P35G-0-14-C) and covered with one or two drops of the appropriate refractive index matching solution, such as BABB. The mounting chamber was not sealed. The samples were imaged using an inverted laser-scanning confocal microscopy system (Zeiss, LSM 880) equipped with a 40x oil immersion lens (Zeiss, EC Plan-Neofluar 40x/NA 1.30) and a 25x water immersion long-working distance objective lens (Leica, 25x/NA 0.95, WD = 2.5 mm). The z-step size was set to 1-2.5 mm.

2.12 Two-photon Confocal Microscopy Imaging

Blood clearing of the DNA origami was observed via intravital imaging of meningeal vessels. The experiment was conducted as described before (Khalin et al., 2020). Briefly, mice were anesthetized intraperitoneally with a combination of medetomidine (0.5 mg/kg), fentanyl 11 (0.05 mg/kg), and midazolam (5mg/kg) (MMF). Fluorescent dyes or DNA origami were applied through a femoral artery catheter. A 4x4-mm cranial window was created over the right fronto-parietal cortex under continuous cooling with saline. The mouse was injected with FITC-dextran (3 µL/g) to visualize the brain vessels and obtain a baseline image. Subsequently, the fluorescently labelled DNA origami solution (1µM, 120 µL) was injected through the femoral catheter. The scanning was performed at 80 µm depth using a laser power of 10% and an 800 nm wavelength. Imaging was carried out with a GAASP detector with an LP<570 nm filter and master gain 600 for the FITC channel, and an LP>570 nm for the origami channel with master gain 600. In total, imaging time did not exceed 70 min. Fluorescence analysis was performed using FIJI software.

2.13 Fluorescent Tomography

Experiments using the IVIS spectrum instrument for optical imaging on mice (Perkin Elmer) were conducted using a protocol similar to that described before (Ponnuswamy et al., 2017). A volume of 100 µl of Alexaflour 750 and doxorubicin with or without DNA origami or 6A10 antibody at a concentration of 0.5 µM was injected. After 2 hours of injection, the mice were anesthetized with ketamine/xylazine and immediately transferred to the imaging system. Using the same setup, we imaged the same animals after vDISCO clearing. Images for kinetic analysis were taken by a 30 s excitation at 745 nm and emission at 800 nm.

2.14 Reconstructions of Whole-body Scans

The reconstruction of whole-body scans is crucial for the visualization and analysis of complex biological systems. In this study, we utilized light-sheet microscopy to acquire image stacks of the entire mouse. To obtain image stacks, we used ImSpector, a software tool developed by LaVision BioTec GmbH, which allowed us to capture high-quality images. The acquired images were saved in 16-bit grayscale TIFF format for each channel separately, ensuring that the images were suitable for further analysis and processing. The reconstruction process involved stitching the image stacks using Fiji (ImageJ2) and fusing them using Vision4D (Arivis AG). The segmentation of organs was done manually by defining regions of interest (ROIs). The segmentation was performed using Imaris (Bitplane AG) and Vision4D. Volumetric and maximum intensity projection were done to obtain the data visualization and color mapping. To stitch mesoSPIM images, we used Terastitcher (Bria and Iannello, 2012). The visualization of the stitched whole-body image and maximum intensity projection was done using Imaris. Our approach allowed for the reconstruction of the entire mouse and accurate segmentation of organs for detailed analysis.

3.   Results

3.1.1 *In Vitro* Stability

To evaluate the stability of the coated DNA nanorods, we incubated them in 5% and 80% mouse serum containing PBS for 24 hours after folding in MgCl2. Subsequently, we imaged the DNA origami rods under TEM at 2500x magnification. Our results showed that the DNA origami rods were observable after 5% serum incubation (Figure 14), and rods were stable in 80% serum-containing PBS (Figure 14).
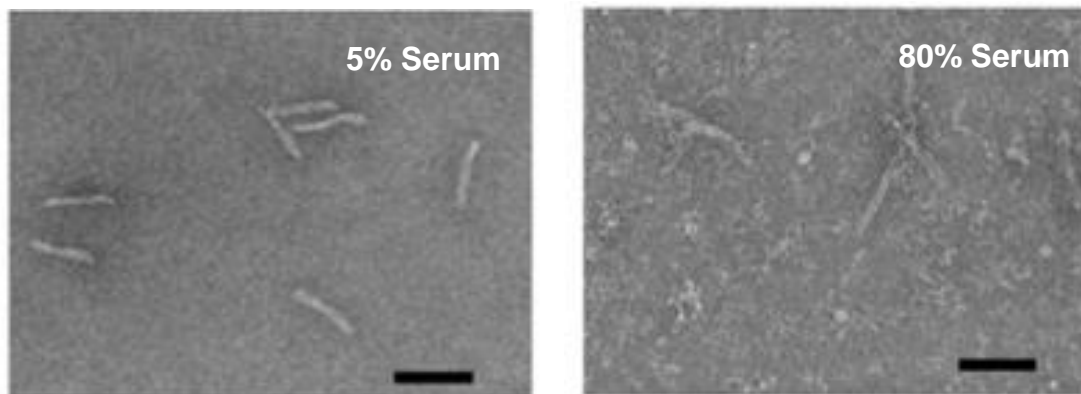
Figure 15: Negative stain transmission electron microscope (TEM) micrograph of the DNA origami rods stabilized with PEG-polylysine and incubated in mouse serum (5% (left), 80% (right), at 37°C, 1h, 50-fold diluted for grid preparation). Scale bar: 100 nm.

3.1.2 DNA Origami Targeting Through Antibody Conjugation Proof of Concept

To demonstrate the potential of DNA origami particles for *in vivo* targeting, we conducted chemical reactions to conjugate 1 or 4 goat anti-mouse CX3CR1 IgG, using the Jonas handle sequence (TGCCTAATCTCTACCTACTCTACTGC). We confirmed the conjugation of each DNA nanorod with CX3CR1 antibody through TEM imaging at 2500x magnification (Figure 15), which directed the DNA origami particles towards binding to monocytes and macrophages. To detect DNA origami *in vivo*, it was coupled with 4 Atto 647 dyes, two in the middle and two at the end.

A

B
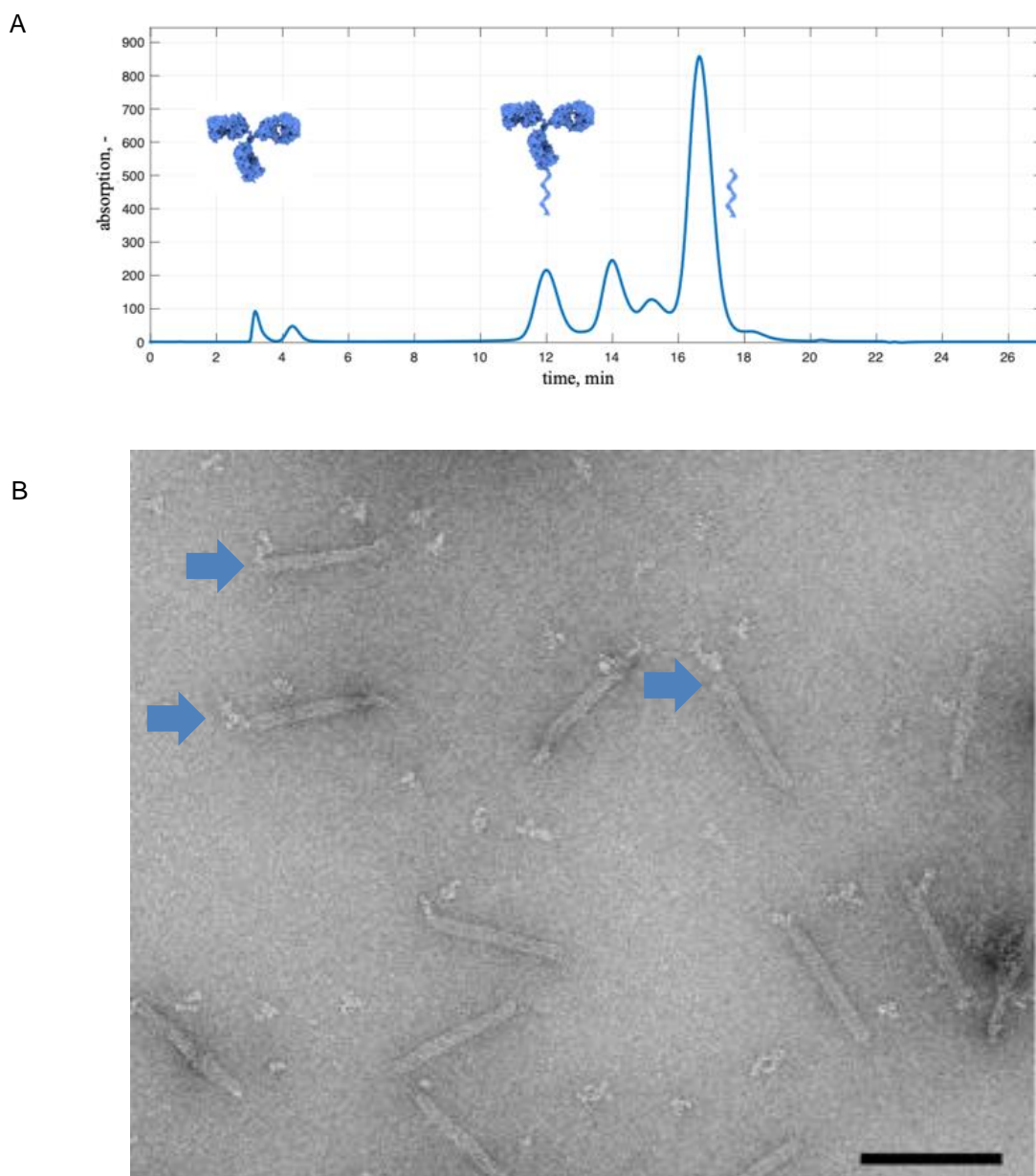
Figure 16: Purifying IgG antibody and single-stranded ssDNA coupling reaction via anion exchange chromatography. **(A)** The chromatogram's peak between 2.5 and 5 min corresponds to the unmodified antibody. The peak at 12 min corresponds the antibody modified with one ssDNA strand, which represents the product of the coupling reaction. At 14 min, the antibody modified with two DNA strands appears as a byproduct. The peak at 17 min corresponds to the unreacted DNA present in excess. **(B)** TEM micrograph of nanorod with one IgG antibody attached .Scale bar 100 nm. The covalently bound antibody at the end of DNA origami nanorods can be observed, blue arrow.

3.2   Protein Corona of DNA Origami

We investigated the protein corona of untargeted DNA origami and immune-targeting DNA origami in Hepes buffer and different concentrations of serum, 70%, 90%, and 100% (Table1 and 2). Our results showed that DNA origami in different concentrations of serum has a slightly bigger size than its solution in Hepes buffer (see blue arrow) (Figure 16). However, DNA origami did not show any aggregation. These findings suggest that our PEGPLys-coated DNA nanorods are stable *in vitro*, and our immune-targeting strategy has the potential for *in vivo* targeting of monocytes and macrophages.

Table 1: Size and zeta potential of untargeted DNA origami

Untargeted origami	Hydrodiameters/nm	PDI	Zeta potential/mV/
Hepes buffer	17.4 ± 0.52	0.12 ± 0.05	-4.1 ± 0.41
70% serum	23.5 ± 0.26	0.20 ± 0.04	-6.8 ± 0.81
90% serum	23.9 ± 0.35	0.16 ± 0.07	-7.1 ± 0.54
99% serum	24.0 ± 0.39	0.18 ± 0.06	-7.2 ± 0.49

Table 2: Size and zeta potential of immune-targeting DNA origami

Immune-targeting origami	Hydrodiameters/nm	PDI	Zeta potential/mV
Hepes buffer	21.5 ± 0.29	0.17 ± 0.03	-5.0 ± 0.30
70% serum	26.5 ± 0.52	0.14 ± 0.02	-7.6 ± 0.76
90% serum	26.9 ± 0.24	0.19 ± 0.05	-8.1 ± 0.69
99% serum	26.8 ± 0.38	0.16 ± 0.08	-8.1 ± 0.46
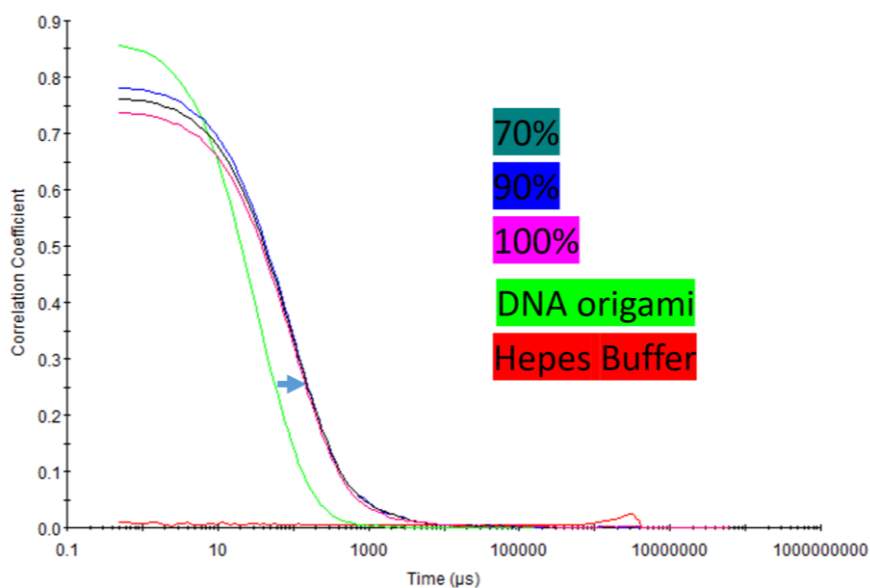
Figure 17: Size of untargeted DNA origami in Hepes buffer vs. in different concentrations of serum

3.3 Bio-distribution of Naked Origami Rods

In our previous work, we developed the vDISCO clearing technology, a method to visualize individual fluorescent cells in whole mice (Cai et al., 2019). To investigate the biodistribution of DNA origami, we injected Atto647 conjugated and PEGPLys coated DNA origami through the femoral vein to CX3CR1GFP-/+ mice. After 20 minutes, DNA origami primarily accumulates in immune organs, such as lymph nodes (pink rectangle), spleen (blue rectangle), and the liver (yellow rectangle) (Figure 17). The zoom-in plane section images of the lymph node, lung, liver, and spleen

exhibit high-resolution DNA origami detection within the internal organs (Figure 26). The distribution of DNA origami on the 640nm channel (red) reveals its specific localization in the lymphatic system and reticuloendothelial system. Overall, our findings suggest that DNA origami could be a promising tool for targeted delivery of therapeutic agents to immune organs. Our vDISCO technology could also provide a non-invasive method for biodistribution studies in preclinical research.
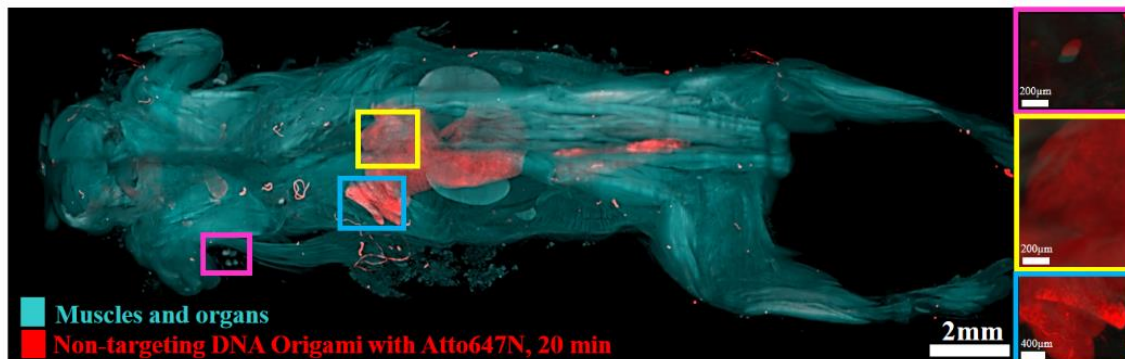
Figure 18: Whole body of DNA origami injected animal cleared with vDISCO without boosting. The auto fluorescence of muscles and internal organs scanned at 488 nm is used to highlight the shape of the whole mouse body in each example (cyan). The naked DNA origami (red) is mainly located in secondary immune organs such as lymph node **(pink),** liver **(yellow)** and spleen **(blue)**. The arrowheads show the origami signal in the organ.

3.3.1 Changes in Origami Distribution over Time

In this study, we aimed to investigate the clearance of DNA origami from the blood and its accumulation in organs as an *in vivo* quality control. To assess the clearance of DNA origami from the bloodstream, we injected naked DNA origami nanorods labeled with Atto550 into C57BL/6 mice through the femoral vein along with FITC-Dextran 2000kDa to label the vasculature. Using a 2-photon microscope, we visualized the meningeal vessels *in vivo* from the moment of injection for 70 minutes (Figure 18). We observed the highest origami signal intensity within 1 minute, which gradually decreased over time. We normalized the signal intensity to the baseline measurement, and the normalized intensity reached zero within 16 minutes (Figure 18).

To test the accumulation of origami in organs, DNA origami was circulated for 20 minutes, 4 hours, and 24 hours before sacrificing and perfusing the animals. After clearing with vDISCO, we imaged the liver using LSFM, as the liver is the main site for the degradation of exogenous particles and had a high signal intensity. After 20 minutes of circulation, we detected DNA origami in the liver and kidney with an ATTO674n signal. However, the signal intensity dropped off after 4 hours (Figure 19), and no signal was observed after 24 hours, indicating the clearance of DNA origami from the organs. Overall, our results demonstrate the efficient clearance of DNA origami from the bloodstream and its minimal accumulation in organs, highlighting its potential as a safe and effective delivery system for therapeutic agents.
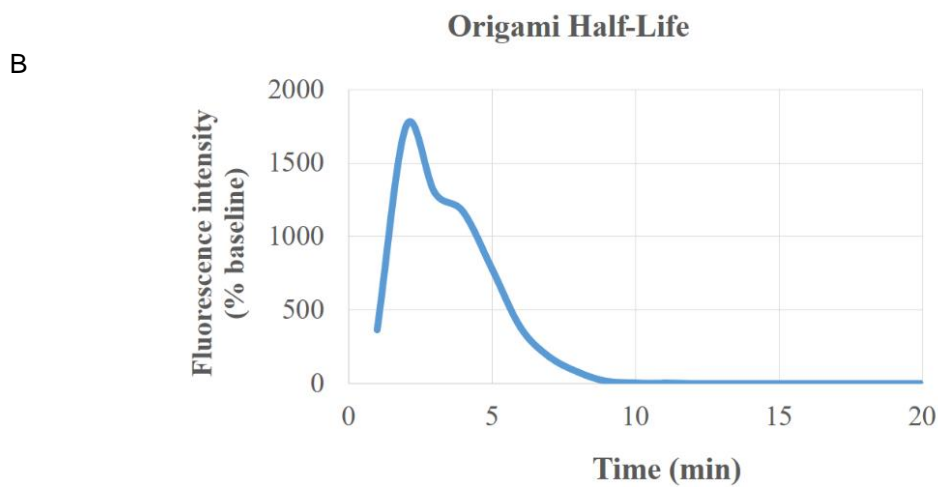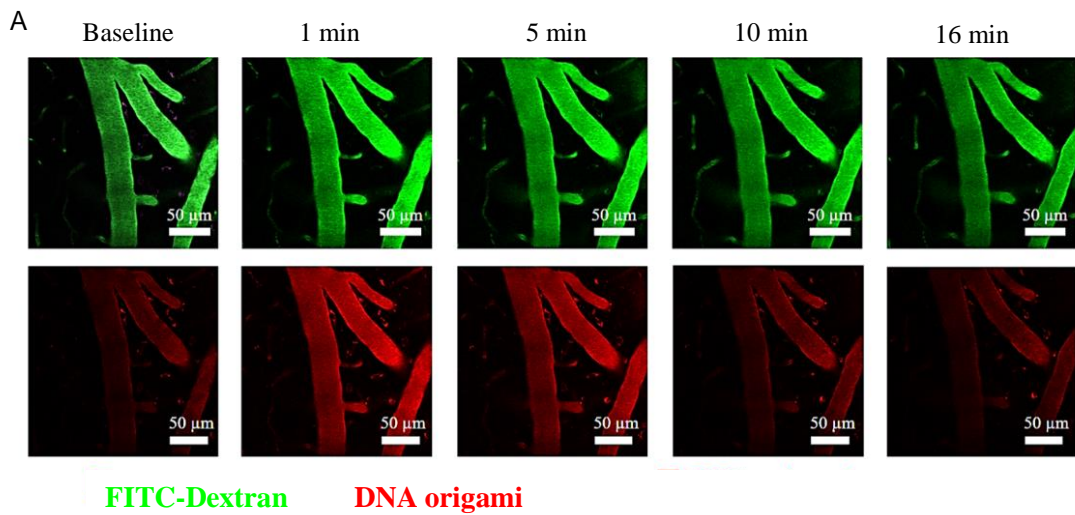
Figure 19: Half-life of DNA origami in blood. (**A**) Blood clearance of naked DNA origami by intravital 2-photon imaging of the meningeal vessels after intravenous injection of FITC Dextran (2000 KDa) (green) to label the vessels and non-targeting DNA origami (red). After the injection of non-targeting origami, the fluorescent signal was recorded for the next 70 minutes. The origami signal immediately increased upon injection and returned to baseline within 16 minutes. (**B**) Quantifying relative intravascular fluorescence intensities over time showed that DNA origami-Atto647 steeply decreased 5 minutes after injection and became negligible after 10 minutes.
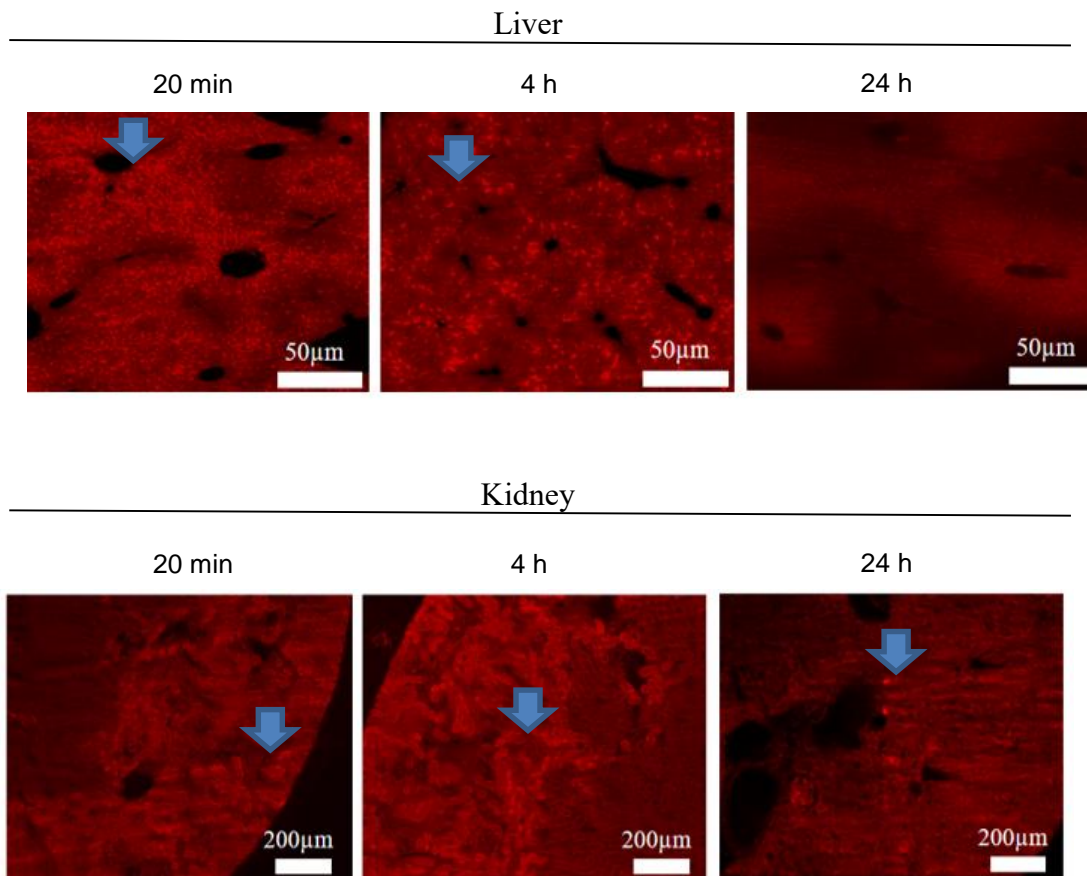
Liver

Kidney

Figure 20: Clearing of DNA origami from the liver and kidney after 20 minutes of circulation, 4 hours and 24 hours after injection through the femoral vein. DNA origami signal is red, pointed with blue arrow.

3.3.2 Immunogenicity Assessments

A significant challenge for the *in vivo* use of nanocarriers is the induction of adverse effects such as excessive immune response. To this end, we assessed the immune safety of DNA nanostructures, as it is critical in the comprehensive evaluation of our DNA origami drug delivery. The immunogenicity assessments addressed the biocompatibility of the DNA origami's inherent properties and any potential influence of the drug delivery process.

As DNA origami is coated with PEGPLys to observe the physiological effects, we administered 400 µL of 2 µM non-targeting, PEGPLys coated DNA origami and only PEGPLys by oral gavage to CD1 animals with mixed genders (n=5). We followed the body weights and sensorimotor function 0, 1, 5, 5, and 7 days after application (Figure 20). These measurements revealed no significant difference in body reaction to DNA origami administration.

We performed an immunophenotypic analysis via flow cytometry and focused on early-activated T cells, characterized by CD45+ CD3+ CD69+, along with the CD45+ CD11b+ monocytes. DNA origami without any particular action to remove residual *E. coli* endotoxins given by tail vein injection induced a substantial immune response: T cells and monocyte numbers highly increased in blood and spleen. In contrast, the purified DNA origami, which had an endotoxins concentration of 0.5 EU/ml, did not induce a significant increase of active T cell or monocyte numbers compared to the mice treated with buffer controls (Figure 21).

In order to test long-term effects of purified and PEGPLys-coated DNA origami, we administrated 400 µL of 2µM purified and PEGPLys-coated DNA origami or PEGPLys alone by oral gavage to mixed gender CD-1 mice (n=5 per group). 24 hours or 7 days later, we collected peripheral blood and spleen immune cell and analyzed them with flow cytometry. We obtained the total T cell count of T cells (CD3+), activated T cells in all T cell populations (CD69+ of CD3+) for adaptive immune

response examination. We also collected monocytes CD11b in CD45+ cell population and activated monocytes (MHCII+ of CD11b+) and compared them with the first data for immune assessment as a chronic phase. There was no significant difference compared to the PEGPLys administrated group in either blood or spleen (Figure 22).

In conclusion, our study suggests that purified DNA origami is immunologically safe.
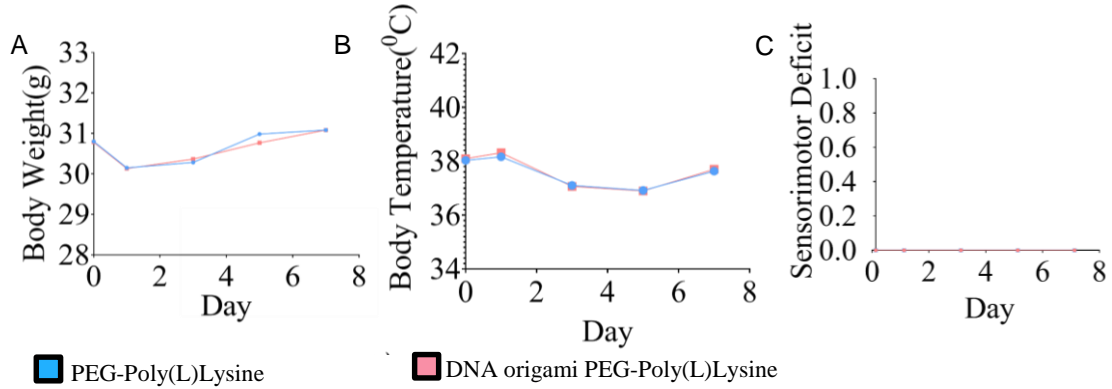
Figure 21: Effects of DNA origami and PEGPLys control administered by oral gavage on body weight **(A)**, body temperature **(B)**, and behavioral score **(C)** on day 0, 1, 3, 5, and 7. Blue represents PEGPLys control and pink represents DNA origami with PEGPLys.
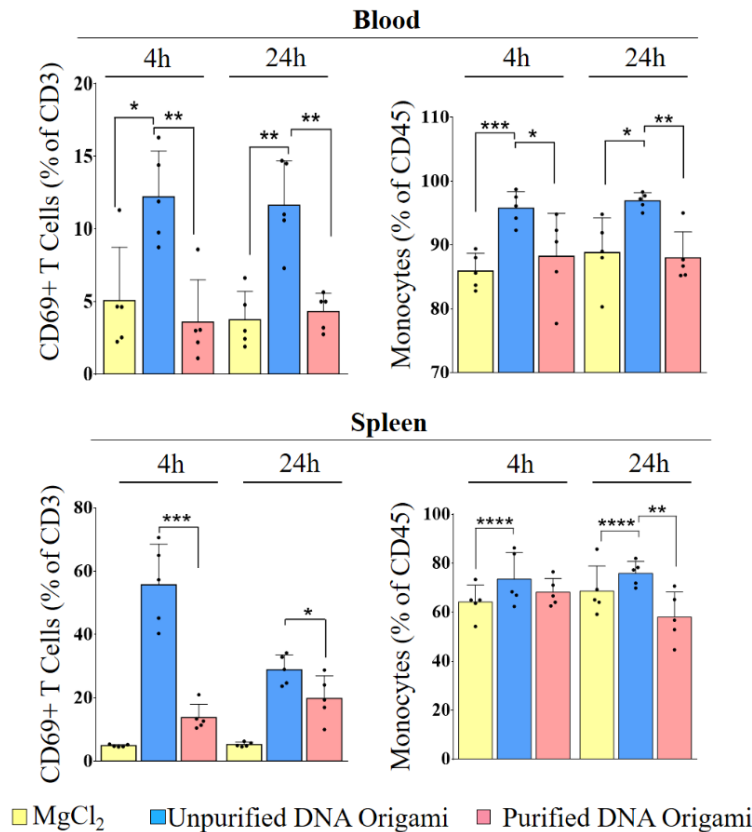
Figure 22: Comparison of the immune reaction between $MgCl_2$ (control), unpurified DNA origami with the folding solution, and purified DNA origami. Comparison of monocytes and activated T cell counts are represented for blood and spleen at acute stage after DNA origami administration through tail-vein injection (n=5). Purification efficiently resolves origami to be immune-tolerable. (*: $p \leq 0.05$, **: $p \leq 0.01$, ***: $p \leq 0.001$, ****: $p \leq 0.0001$)
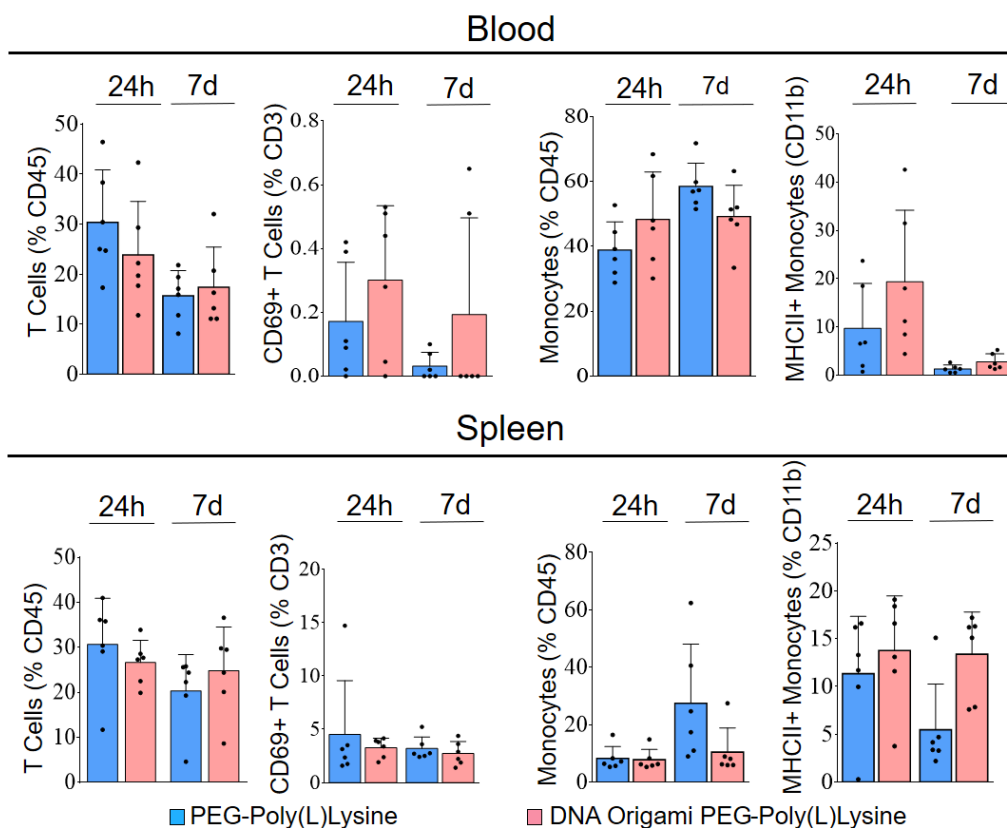
Figure 23: Comparison of monocytes, T cell populations, and their activation in blood and spleen after DNA origami administration: Blue represents PEG-Poly (L) Lysine control and pink represents DNA origami with PEGPLys. There was no statistical significance.

3.4 Central Nervous System Penetration Assessment of Non-targeting DNA Origami

For the assessment of passive translocation of non-targeting DNA origami to the central nervous system, we focused on the brain. Higher magnification imaging revealed that without specific efforts to breach the blood-brain barrier, DNA origami cannot penetrate the brain parenchyma. The fluorescent signal from DNA origami was only observed on the outer surface of the brain and in the ventricles. DNA nanoparticles were detected in the meningeal vasculature and skull bone marrow of animals with a positive origami signal in their liver and spleen (Figure 24).
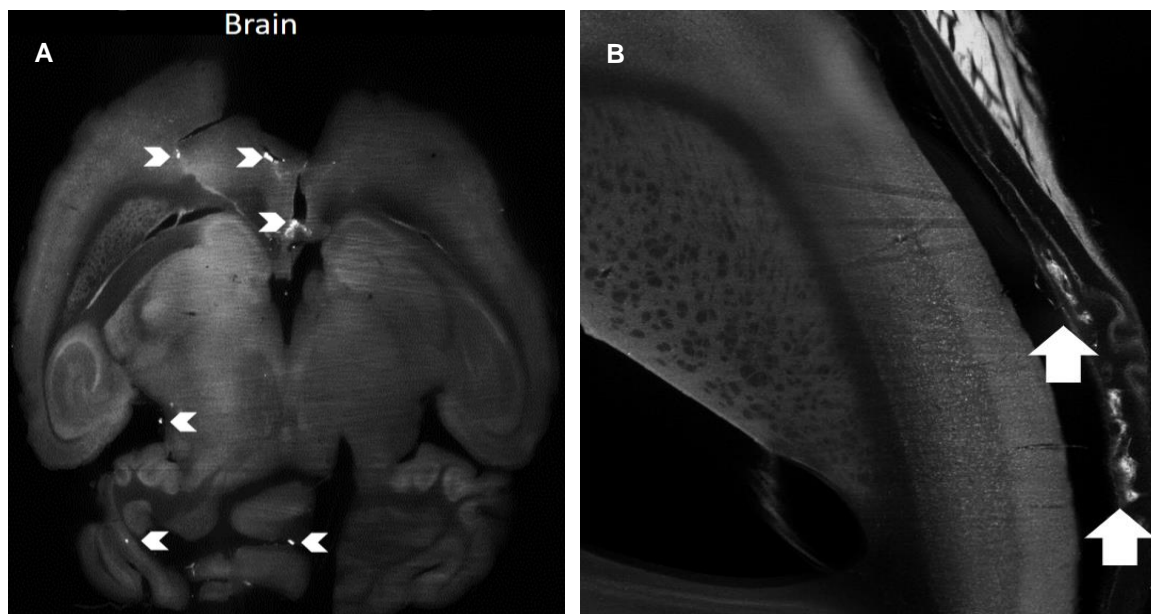
Figure 24: Non-targeting DNA origami cannot translocate to the brain parenchyma. Mice with high signal intensity in the liver and spleen showed no signal in the brain parenchyma. The fluorescent signal from DNA origami was only detected on the outer surface of the brain and in the ventricles **(A)** (white arrowheads), while it was observed in the meningeal vessels and skull bone marrow **(B)** (white arrows).

3.5   Changes in *in Vivo* Distribution of Origami with Targeting

In order to target DNA origami to CX3CR1-positive monocytes/macrophages, we conjugated them to a goat anti-mouse CX3CR1 antibody. For comparison, we used DNA origami coupled to the human carbonic anhydrase (CA) XII-specific antibody (6A10). Both types of origami were coated with PEGPLys to improve their stability. CX3CR1 antibody-conjugated DNA origami were injected into CX3CR1GFP-/+ mice via the tail vein and mice were sacrificed after 20 minutes. After applying vDISCO without boosting and imaging with LaVision Ultramicroscopy II, we merged all channels for comparison.

The distribution of DNA origami conjugated to a goat anti-mouse CX3CR1 antibody in the 640nm channel (red) revealed that it is primarily concentrated in immune organs such as the lymph node (pink rectangle), spleen (yellow rectangle), and liver (blue rectangle) (Figure 23). Overall, these findings suggest that DNA origami has potential as a targeted drug delivery system, and further research in this area could lead to significant advancements in medicine.
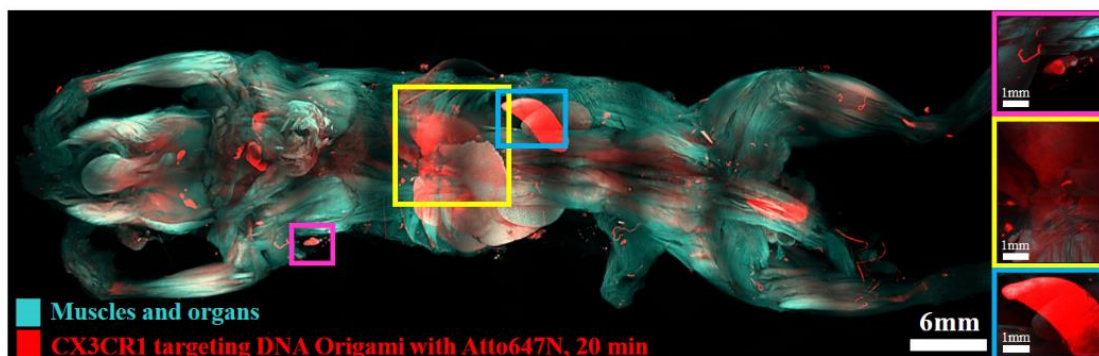
Figure 25: CX3CR1 antibody conjugated DNA origami injection to mice through femoral vein and vDISCO clearing without boosting. CX3CR1-targeting directs DNA origami to monocytes, macrophages and microglia. The red DNA origami signal is mainly located in monocyte and macrophage populated lymph node **(pink),** liver **(yellow)** and spleen **(blue).**

We further evaluated the effectiveness of the DNA origami-6A10-Atto555 complex as a targeted delivery system for breast cancer metastases. We measured the metastases with biolumines-cence (Figure 24) and observed that 6A10 antibody targets and binds to MDA-MB-231 cells. After applying vDISCO with boosting mCherry of the tumor cells to far-red spectra and imaging with LaVision Blaze Microscopy, we merged all channels for comparative representation. We observed that the cancer metastasis was detectable in many internal organs, including the lung, liver, and kidney (Figure 24 and 25).The distribution of DNA origami in the whole body revealed a different pattern compared to the non-targeting or CX3CR1 antibody-conjugated DNA origami. The DNA origami did not accumulated in immune organs but located particularly in the lungs where breast cancer metastases occurred (Figure 25). These findings indicate that DNA origami has the potential to be an effective targeted delivery system for breast cancer metastases.
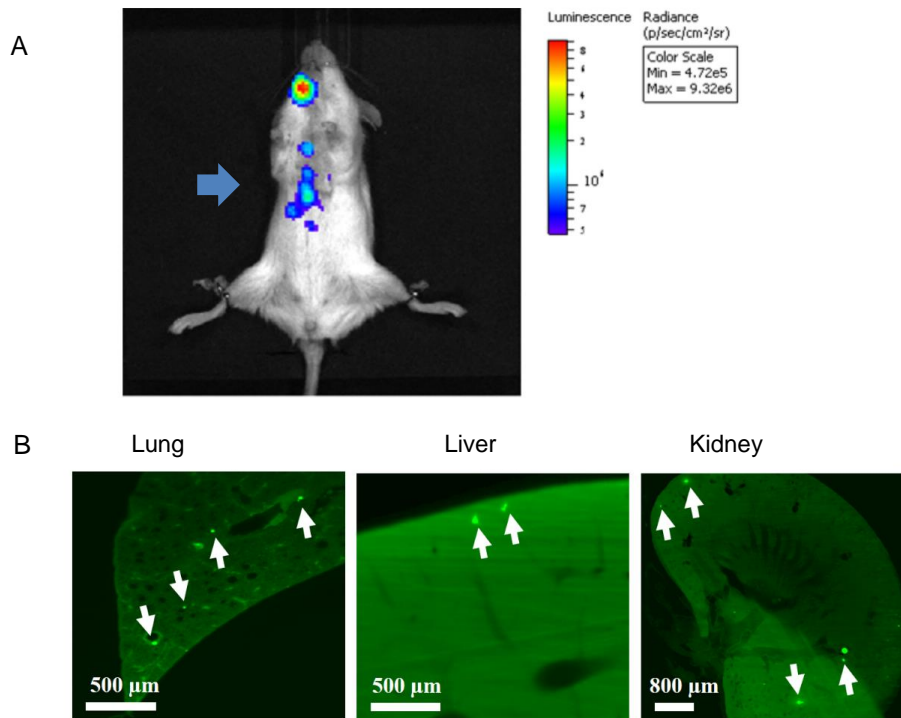
Figure 26: Cancer distribution assessment. While bioluminescence imaging can provide *in vivo* information **(A)**, it is lack of single cell resolution that is provided by vDISCO **(B).** Bioluminescence images of a female NSG mouse were taken two weeks after application of Luciferin expressing MDA-MB-231 cancer cell (blue arrow) **(A)**. We identified single micrometastases in the internal organs such as the lung, liver and kidney **(B)**. MDA-MB-231 cells are green.
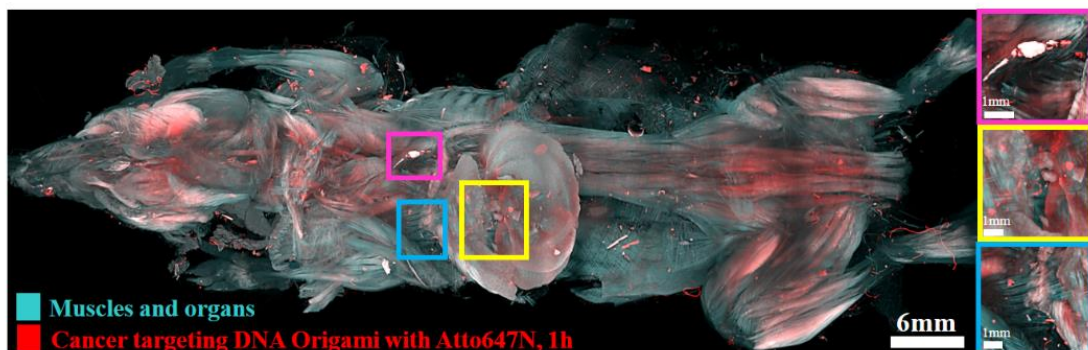
Figure 27: Cancer-targeting (6A10 antibody conjugated) DNA origami biodistribution assessment and 3D visualization of the transparent mouse body. We identified both origami in lung **(pink and blue)** and liver **(yellow)**. DNA origami is in red. As the heart is the location of primary tumor and has high intensity signal, it was removed before imaging to prevent masking the lungs.

Focusing on the lung, liver and spleen of cleared mice, we compared the signal intensity of different modalities of origami (Figure 26). ATTO647 dye with oligonucleotides, which were used for labeling origami, cleared from the organs quickly (Figure 26). Non-targeting origami was present only in the liver and spleen but not in the lungs (Figure 26). We detected goat anti-CX3CR1 conjugated origami signal in the liver and spleen with more tissue penetration (Figure 26). Rat 6A10 conjugated DNA origami signal was absent in the liver and spleen. However, signal in 561 nm channel from rat anti-6A10 conjugated DNA origami is located mainly in lungs, where the main cancer metastasis locates (Figure 26). The principal organs of other origami modalities had signals.
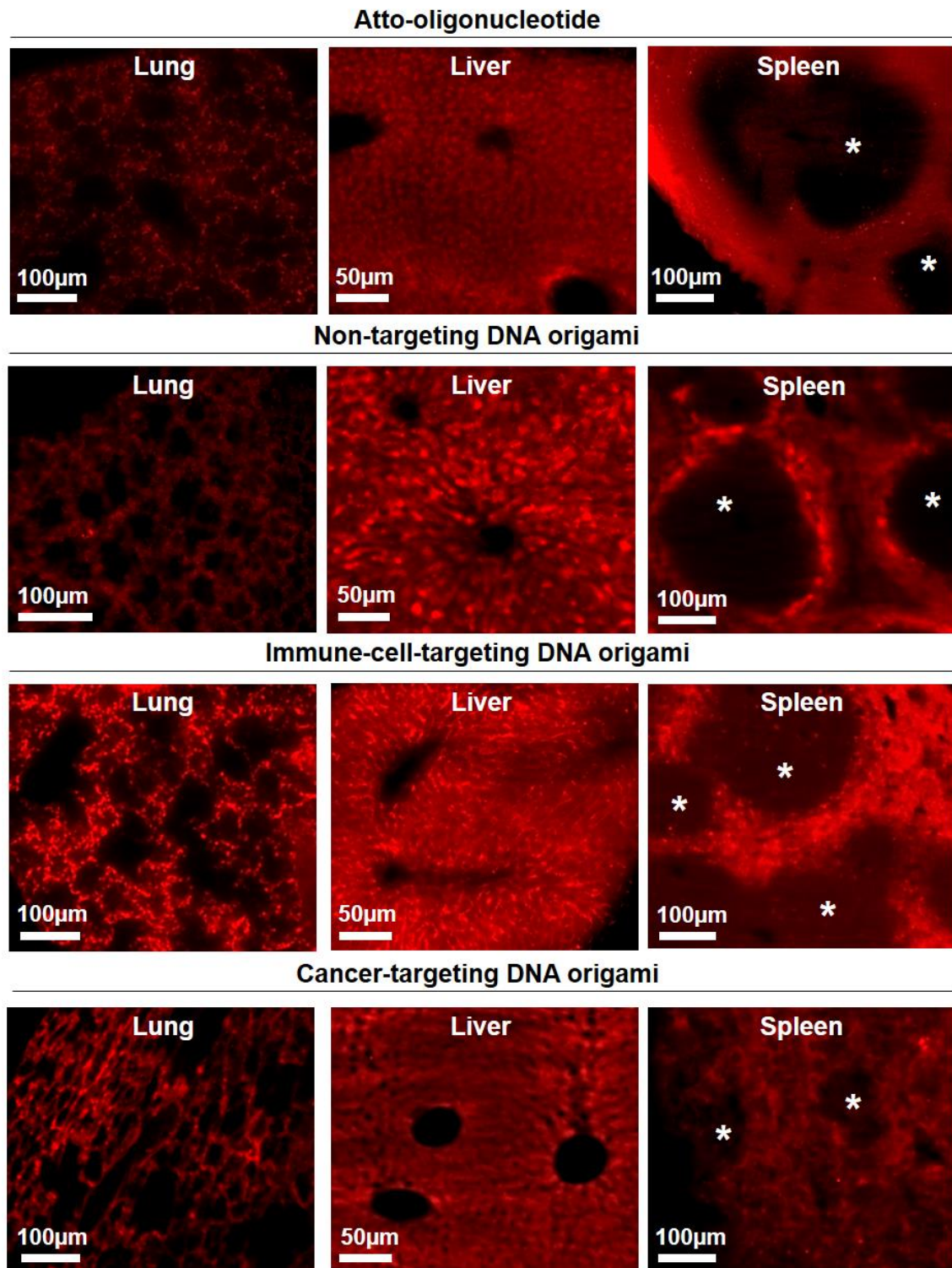
Figure 28: Distribution of DNA origami with different targeting moieties in selected organs. Red signal represents Atto dye with or without DNA origami. The asterisks point to the signal-free white pulp of the spleen. Blue arrows show the red signal from the Atto dyes on DNA origami. Atto-oligonucleotide cleared from the organs quickly, therefore, no signal was observed. Non-targeting origami was present only in the liver and red pulp of spleen but not in the lungs. Immune-targeting origami could be detected in all tissues with monocytes/macrophages. Cancer-targeting DNA origami is located mainly in lungs, where the main cancer metastasis locates.

To compare targeting efficiency, we injected cancer-targeting DNA origami in tumor-bearing and healthy animals. We also injected 6A10 cancer-targeting antibodies and non-targeting DNA origami into tumor-bearing animals (Figure 27, 28). As reported before, cancer-targeting DNA origami is observable in lung and metastatic tissues, mainly the liver. With the same concentration of 6A10 antibody, the distribution seems more random and dispersed. Mainly spleens accumulated non-targeting origami. In the absence of cancer cells, cancer-targeting origami is observable in the liver, which seems to be random and to be for elimination (Figure 28).

Tumor-bearing animal
+
cancer-targeting origami (1 h)
MDA-MB-231
origami

Tumor-bearing animal
+
6A10 (20ug) (1 h)
MDA-MB-231
6A10

Tumor-bearing animal
+
non-targeting origami (1 h)
MDA-MB-231
Non-targeting origami

Healthy animal
+
Cancer-targeting origami (1 h)
Cancer-targeting origami
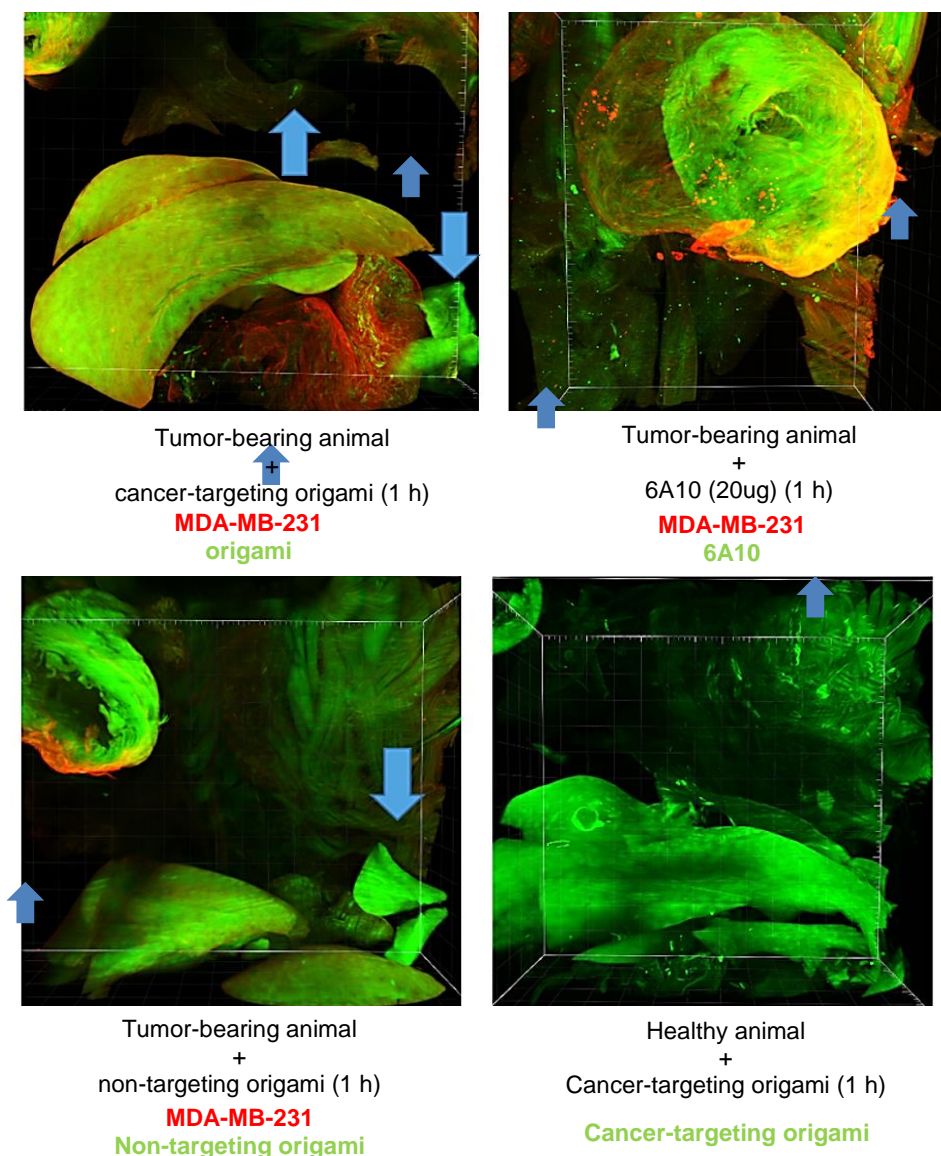
Figure 29: Comparison of bio-distribution and targeting of origami under different conditions. Cancer-targeting DNA origami successfully accumulated in metastatic tissues, mainly the lung and liver. The distribution of 6A10 seemed more random and dispersed so that can be observable in all organs. Especially liver had a surfeit antibody signal, which might cause toxic accumulation. A large amount of non-targeting origami accumulated in the spleen after one hour circulation. As suggested before, this might be the result of time-dependent behavior. We observed cancer-targeting origami in the liver, where it could be metabolized down and cleared from the body in the healthy group when no cancer cells were present.
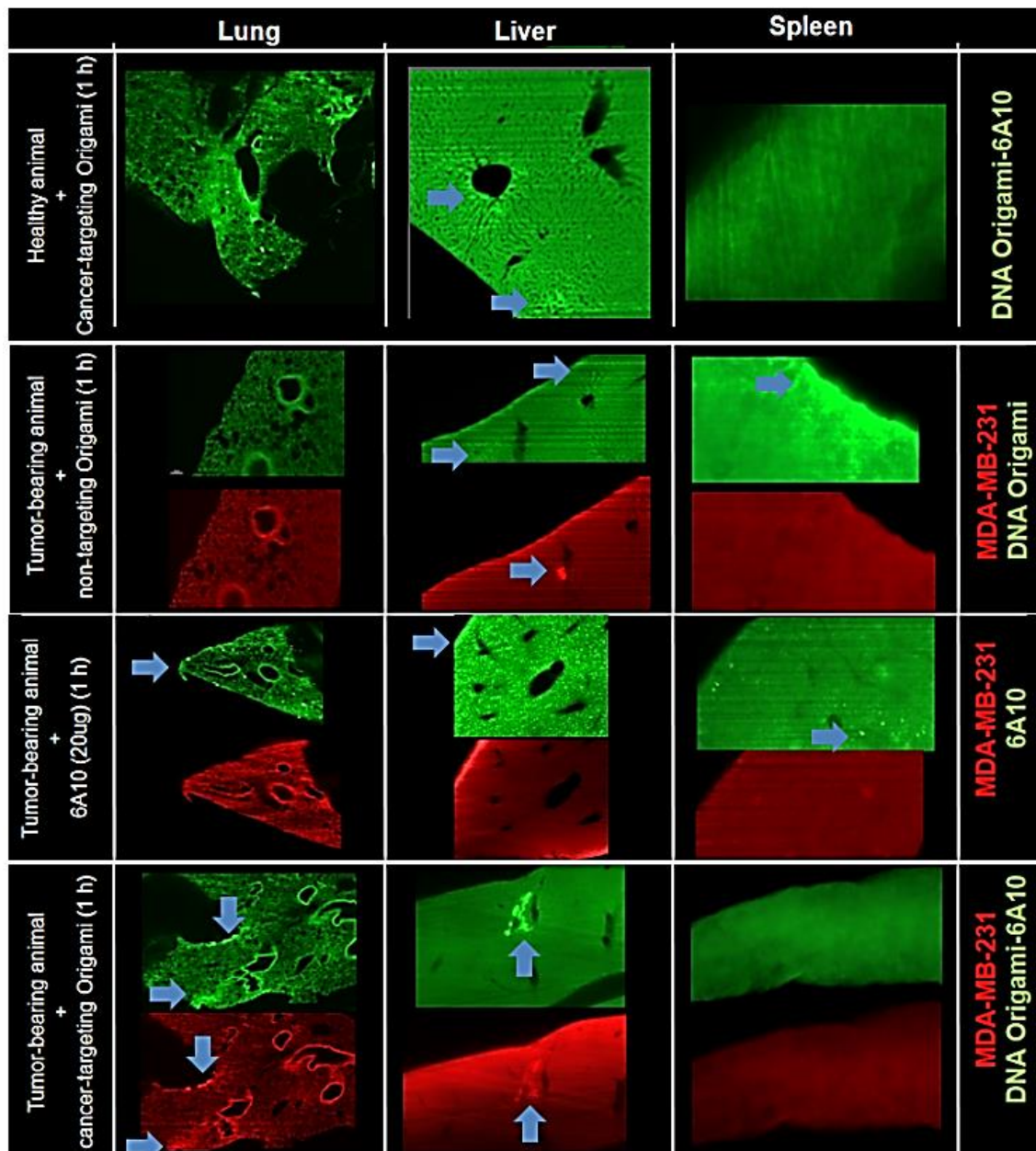
Figure 30: Comparison of organ distribution of origami under different conditions. Zoom-in comparison of different DNA origami moieties in different conditions. Blue arrows show the detected signal. In the healthy group, cancer-targeting origami was observed in the liver, where it was metabolized and cleared from the body. A significant accumulation of non-targeting origami was observed in the liver and spleen, even though co-localization could not be detected. Cancer-targeting DNA origami successfully accumulated and overlapped in metastatic tissues, particularly the lung and liver, while the distribution of 6A10 appeared more random, being observable in all organs.

3.5.1 Cellular Targeting of Antibody Conjugated DNA Origami

In order to investigate the distribution patterns of different origami constructs, we performed sub-cellular level analysis of cleared tissues using confocal microscopy, after identifying the constructs at the whole mouse and organ level. Our findings revealed that the non-targeting and immune-cell-targeting DNA origami signals had distinct distribution patterns in liver tissue. Specifically, the non-targeting origami localized mainly within the liver sinusoids, which are rich in endothelial cells and Kupffer cells responsible for drug translocation to hepatocytes - the site of drug metabolism (Figure 29). On the other hand, the immune-cell-targeting DNA origami showed a similar distribu-

tion pattern to the non-targeting origami, but with higher signal intensity and deeper tissue penetration, suggesting better retention of the DNA origami when conjugated with immune cell-targeting antibodies (Figure 29). Additionally, Kupffer cells are CX3CR1 positive and attached to sinusoids' walls. Therefore, another interpretation is that; immune cell-targeting DNA origami are localized in the same region (Figure 29).

To obtain detailed, sub-cellular information on the localization of DNA origami, we performed immunohistochemistry on tissue sections with antibodies targeting either CX3CR1 or CD68 antibodies. CD68 is the marker for lysosomal and endosomal vesicles. With this labeling, we can differentiate the internalization method of DNA origami through either receptor turnover or random phagocytosis. The non-targeting origami displayed co-localization with CD68, mainly located within the cells, while the CX3CR1 conjugated DNA origami co-localized mostly with CX3CR1 positive cells (Figure 30). Internalization of the immune-targeting DNA origami suggest a successful uptake of the origami-CX3CR1 antibody couple upon receptor turnover (Figure 30). Moreover, our data demonstrate that cancer-targeting origami conjugated with 6A10-antibody successfully targets and internalizes into cancer cells in various organs, including the lung and liver. The specificity and selectivity of DNA origami technology make it a promising tool for targeted drug delivery.
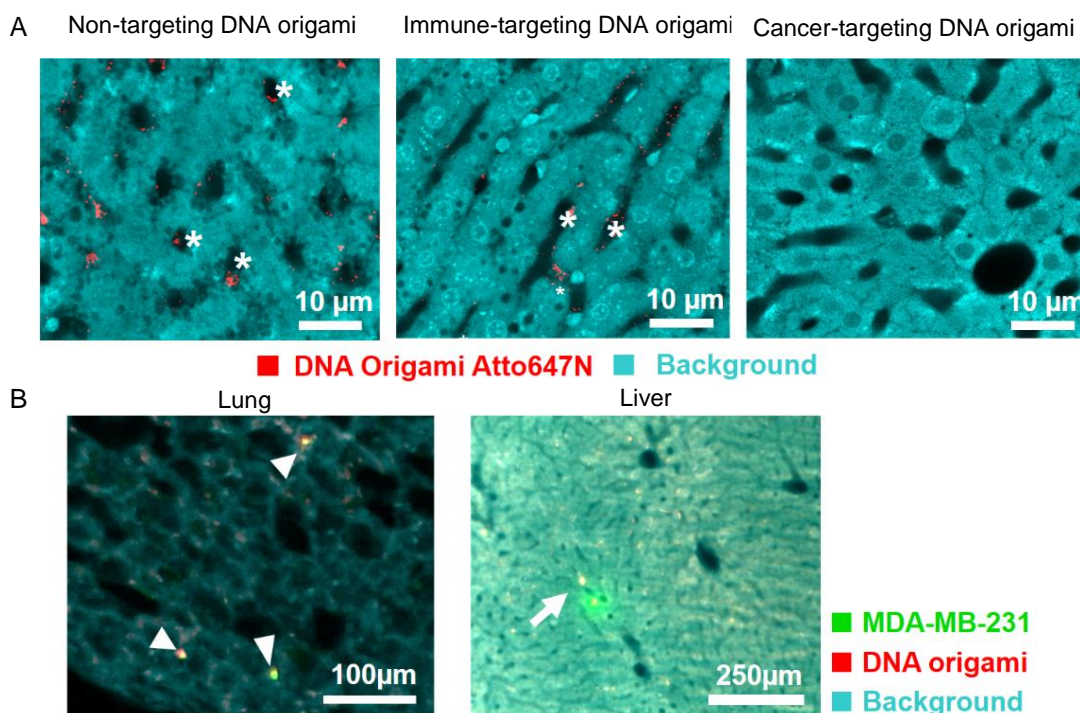
Figure 31: Comparison of the cellular localization of different DNA origami. Confocal images of liver from on-targeted, CX3CR1 targeting and 6A10 conjugated origami **(A)**. The background is blue and DNA origami signal is red. The asterisks point the liver sinusoids, which is a type of capillary with a lining of endothelial cells and Kupffer cells (CX3CR1+). The non-targeting and immune targeting DNA origami signal can be detected in liver sinusoids, whereas cancer-targeting DNA origami was not detected in the liver after 1h circulation. Cancer targeting efficiency of DNA origami **(B).** The images from the lung and liver showed that the DNA origami signal overlaps many regions with cancer metastases (arrow), and there are some non-targeted MDA-MB-231 cells (arrowhead).
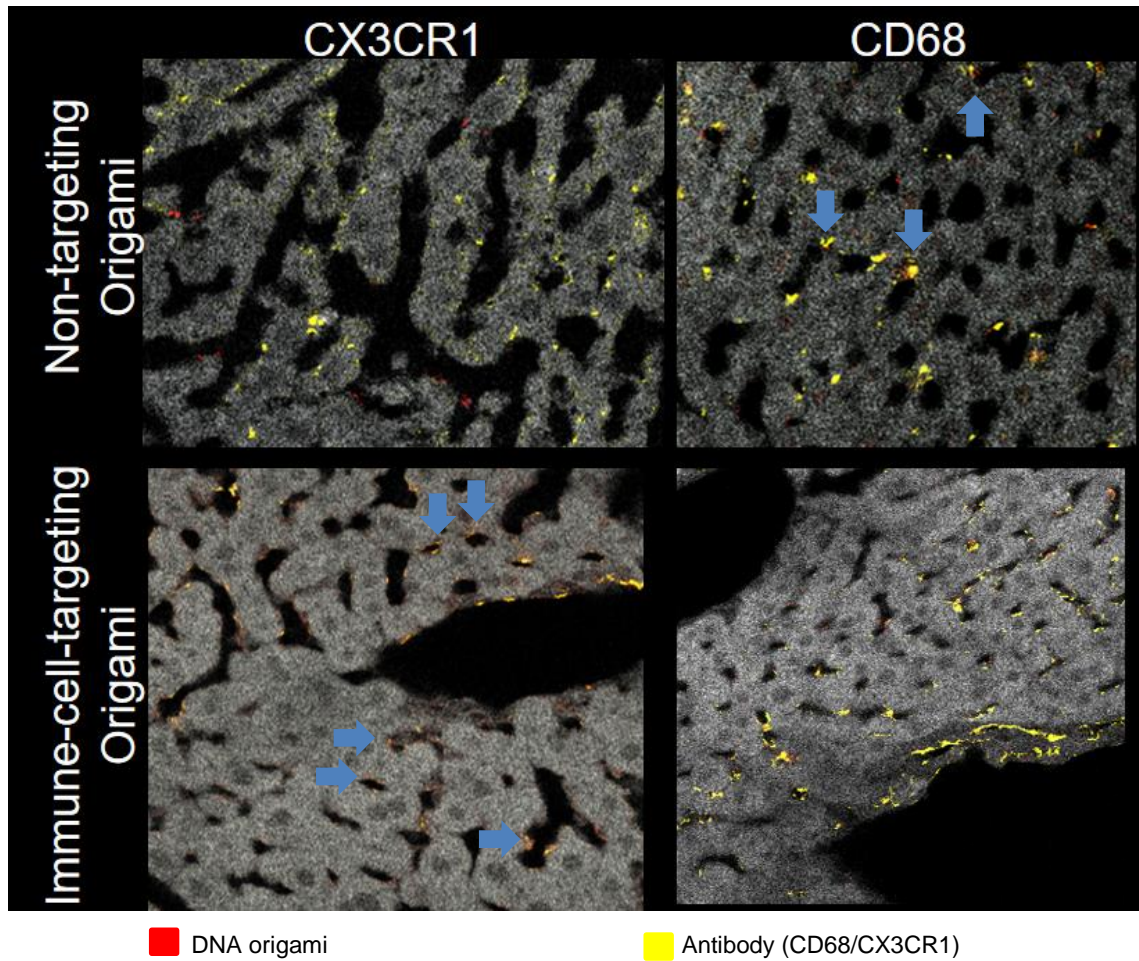
Figure 32: The comparison of the localization of DNA origami in comparison with CX3CR1 and CD68 in liver. The background is grey, antibody is yellow and DNA origami signal is red. When DNA origami was non-targeting, it co-localized with CD68, the vesicular marker of phagocytotic cell, more than it colocalized with CX3CR1. In contrast, in the lower panel, immune-cell-targeting DNA origami upon anti-CX3CR1 conjugation enhanced the co-localization with CX3CR1. Blue arrows show the co-localization. This suggest that Kupffer cell localization of non-targeting DNA origami was upon random phagocytosis, however, immune-cell-targeting DNA origami actively attaches to surface CX3CR1 and encapsulated for receptor turnover.

3.6 Comparison of Previous Biodistribution Techniques with vDISCO Clearing and LSM Imaging

Previous reports showing nanoparticle biodistribution used bioluminescence or fluorescent tomography (Perrault and Shih, 2014a; Zhang *et al.*, 2014; Ponnuswamy *et al.*, 2017). However, these techniques lack the necessary accuracy at the cellular level required for precise evaluation of nanoparticle distribution in whole-body mice. To address this, we employed bioluminescence, fluorescent tomography, and tissue clearing techniques (Figure 31) to achieve a higher level of accuracy in determining nanoparticle distribution. Our results showed that vDISCO and LSFM techniques provided information at both the organ and cellular levels, whereas bioluminescence and fluorescence tomography techniques only provided assumptions about the location of DNA nanoparticles. Additionally, bioluminescence and fluorescence tomography could not detect signals emitted by short-wavelength fluorophores or endogenous proteins such as ATTO550 or eGFP. In contrast, the use of ATTO750 conjugated with DNA origami allowed for detection of a white signal in fluorescent tomography images (Figure 31). However, mCherry signal in the 558nm wavelength was only detectable after vDISCO clearing (Figure 31). Overall, vDISCO and LSFM techniques provided a more accurate and comprehensive view of nanoparticle distribution at both the whole-body and cellular levels.
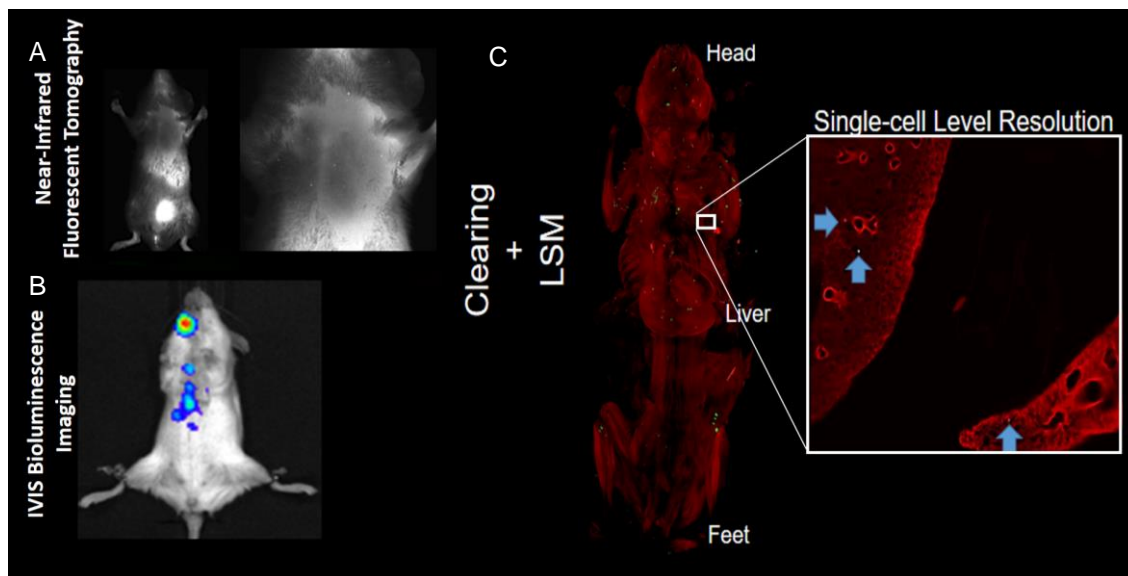
Figure 33: Comparison of imaging modalities with tissue clearing and LSM monitoring. Fluorescence tomography **(A)** and bioluminescence **(B)** techniques only provided assumptions about the location of DNA nanoparticles, whereas vDISCO and LSFM techniques provided information at both the organ and cellular level **(C)**, blue arrows. As clearly shown in the figures, tissue clearing and light sheet microscope imaging can provide single cell resolution whilst bioluminescence and fluorescent tomography can only provide rough estimation of the localization of DNA origami. Additionally, bioluminescence and fluorescence tomography could not detect signals emitted by short-wavelength fluorophores or endogenous proteins such as ATTO550 or eGFP.

3.7   Atherosclerotic Targeting with DNA Origami

Focusing on the heart and aorta of cleared mice, we compared the signal intensity of CX3CR1-eGFP and immune-cell-targeting origami localization. While CX3CR1-positive atherosclerotic plaques were detected, immune-cell-targeting DNA origami signal was notably absent in most lesion areas; limited origami penetration was observed in only one zone of the mitral valve with atherosclerotic lesions (Figure 34). Furthermore, goat anti-CX3CR1-conjugated origami signal was detected in the liver and spleen of the same animals, overlapping with CX3CR1-positive cells (Figure 35).
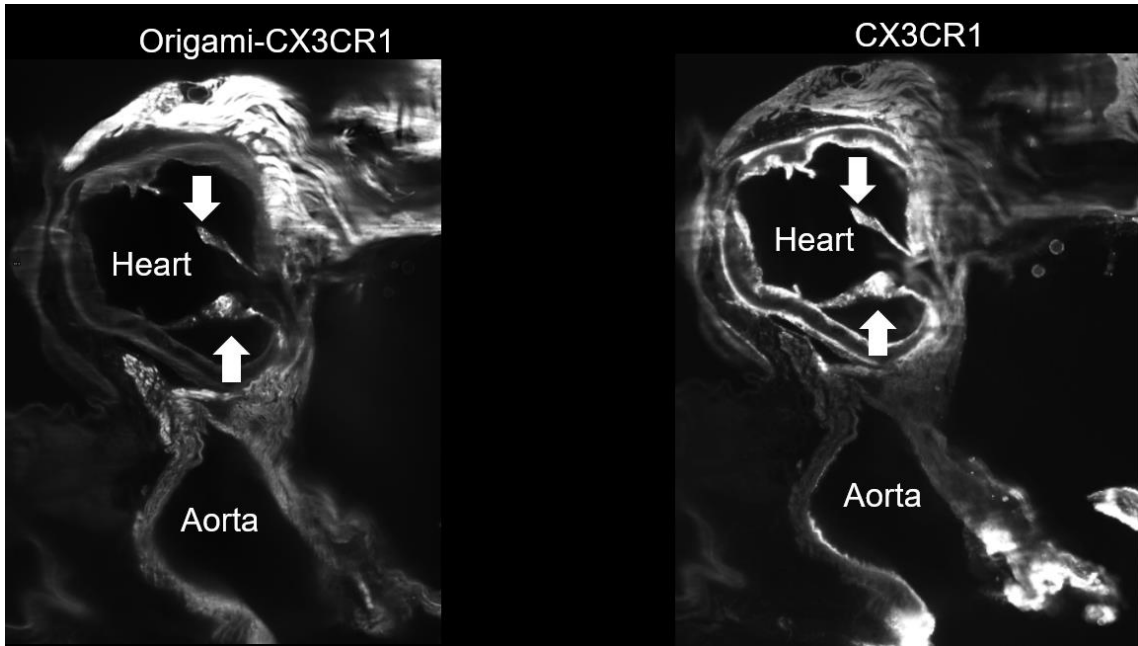
Figure 34: Immune-cell-targeting DNA origami cannot reach to the macrophages at the atherosclerotic site.
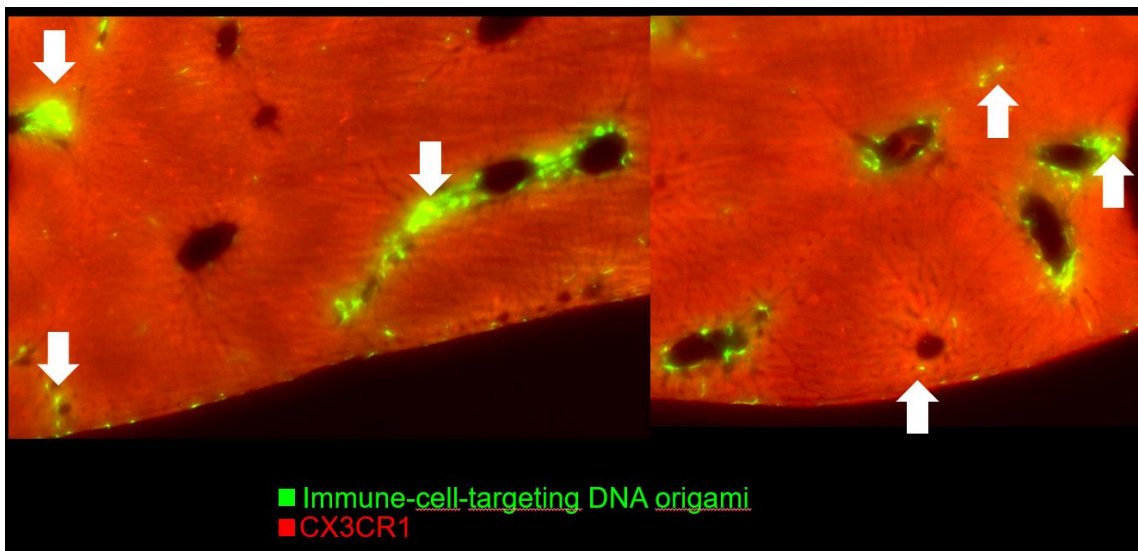
Figure 35: Immune-cell-targeting DNA origami signal overlaps with the CX3CR1+ cells in the liver of atherosclerotic mice.

3.8 Therapeutic Targeting of Cancer for Functional Cargo Delivery with DNA Origami

We investigated the cargo capability of DNA origami by conjugating it with Doxorubicin (DOX), a potent anticancer medication. Systemic administration of DOX can cause an adverse effect, as it is a cell cycle inhibitor. However, conjugation with DNA origami provided a better targeting approach to cancer cells, reducing the off-target effect of DOX. Moreover, we utilized DeepMACT quantification, an unbiased method, to evaluate the effects of DNA origami-DOX conjugates on cancer metastasis. Our results showed that DNA origami conjugated with DOX had a greater impact on metastatic cell counts, indicating the potential of this system for targeted cancer therapy (Figure 32).

	DNA origami-DOX (0.25mg/kg)	DOX (0.25mg/kg)
Total Cancer Count	184	304
Lung+Heart	140	215
Liver	44	89
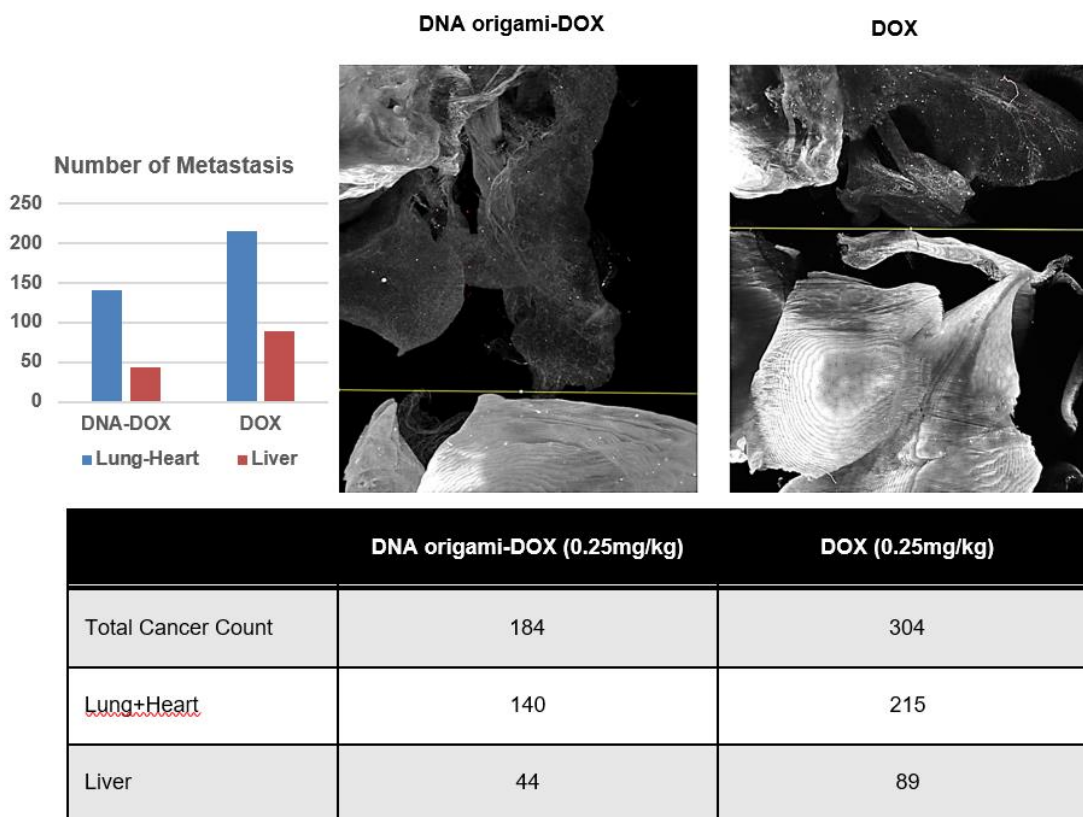
Figure 36: DeepMACT quantification of cancer metastasis. Comparison of treatment with Dox and DNA origami conjugated with Dox. The conjugation of DOX with DNA origami increased the anti-cancer effect.

4. Discussion

DNA origami has emerged as a promising nanotechnology for improving the specificity and targeting of therapies. While several nanoparticles have been developed in nanomedicine, only a few have advanced to clinical applications. DNA origami nanoparticles offer several advantages, such as modularity, biocompatibility, high load capacity, structure flexibility, and precise control during construction (Wang et al., 2017). In our study, we evaluated the safety, biodistribution, clearance, and targeting efficiency of engineered DNA origami rods using advanced whole-body imaging technologies (Cai et al., 2019; Pan et al., 2019b).

Previous research has shown that different DNA origami shapes exhibit different dynamics, with shape-dependent localization and early immune activation observed in myeloid lineage cells. The kinetics and level of the immune response also depend on the administration route, particularly in peripheral blood (Lucas et al., 2022; Zhang et al., 2014). Our study focused on a simple and typical DNA origami structure, which can be produced quickly and inexpensively in high amounts. We used this structure to create different moieties, comparing their modifications through the same administration route. While our study provides a proof-of-concept investigation, further research is needed to explore the potential of different DNA origami shapes and administration routes in improving the efficacy of nanomedicine.

In this study, we aimed to assess the pharmacological efficiency of DNA origami through *in vitro* assessments for producibility, stability, and conductibility. Previous work has shown that DNA origami can be produced in high quantities with robust formulation (Praetorius *et al.*, 2017). To assess the stability of DNA origami, we investigated its denaturation and aggregation using TEM and 2-photon imaging, respectively. The results showed that DNA origami was stable both *in vitro* and *in vivo* and it was cleared from the systemic circulation within 15 minutes, accumulating in peripheral organs.

Intravital observation of meningeal blood vessels for 70 minutes revealed no accumulation of DNA origami in the vessels or any interaction with immune cells during circulation. Our findings are consistent with a previous report that coated particles clear more slowly than uncoated DNA nanoparticles with a half-life of 45 min and show a higher signal in the liver (Ponnuswamy et al., 2017). However, our PEGPLys coated DNA origami cleared much faster than reported, which could be due to the shape and coating material, altering the clearance of the particle. We also assessed the therapeutic persistence of DNA origami, including the presence of potential impurities, antibodies against the therapeutic, and any delayed or acute reactions, such as T cell activation. Our results showed that DNA origami has potential as a stable and conductible therapeutic agent. Overall, DNA origami holds great promise as a novel drug delivery system, with unique properties such as high load capacity, structure flexibility, and precise construction control (Shakhnovich et al., 2020; Wang et al., 2017).

The second step in our investigation was the assessment of biocompatibility and safety for medical usage. For that purpose, we evaluated the immune response to the administration of different DNA origami moieties and monitored the immune cell population in peripheral blood and spleen, tissue integrity, and behavior. We did not observe any advert effect in the tissues or the behavior of mice independent of the route of application, i.e. systemic or oral. We did not detect any tissue defect, physiological alteration, or behavioral change at the acute and chronic phases, regardless of antibody conjugation. Previously, a few other studies have also been conducted to examine *in vivo* immunogenicity (Surana, Shenoy and Krishnan, 2015; Lucas *et al.*, 2022), all of which concluded, too, that DNA origami is immune tolerable. There has been toxicological proof that DNA origami treatments *in vivo* are nontoxic even in response to repeated dosing at a high amount (Lucas *et al.*, 2022). Our findings correlated with previous biosafety assessments.

We manufactured DNA origami in *E. coli*; therefore, the final solution was contaminated with endotoxins, and bacterial lipopolysaccharides (LPS). Thus, there was a high possibility of an im-

mune reaction due to the endotoxins. As a bacterial substance, endotoxin induces pro-inflammatory activity *in vivo* applications. Hence we had to remove them (Chen, Ross and Hambardzumyan, 2019). In order to make DNA origami immune tolerable, we also explored the effect of purification. According to the immune cell counts, an additional purification step before *in vivo* application improved the immune tolerance, proving the efficiency of the purification step.

In this study, we used our recent technologies to provide a scalable and unbiased histological assessment of entire biological specimens to understand the *in vivo* behavior of Origami. Over the past 20 years, many nanoparticles have been found to have relative tissue accumulation in the liver and spleen (Alexis *et al.*, 2008). Non-targeting origami also followed this distribution pattern. Previously, whole-body distribution of DNA origami particles was attempted (Hahn *et al.*, 2014; Perrault and Shih, 2014a; Cuccarese *et al.*, 2017; Ponnuswamy *et al.*, 2017; Lucas *et al.*, 2022). These reports stated that DNA nanoparticles are primarily localized in the liver and spleen. However, spleen localization is mainly after a longer circulation time. We observed exactly the same results. After 20 min of circulation, non-targeting DNA origami was located only in liver. After 1 hour of circulation, the signal in liver retained, but we could also observe signals in spleen. We could explain this distribution pattern with the properties of these tissues. Polymeric nanoparticles' biodistribution and clearance are predominantly influenced by tissue defects, stealth properties, targeting, and nanoparticle size. Additionally, discontinuous endothelium is a characteristic of the liver (fenestrae of 50-100 nm), allowing many nanoparticles and drug molecules to enter these tissues. Furthermore, as evident from its structural characteristics, the spleen is highly permeable to blood-borne molecules. The spleen tissue serves as a distribution site for various medications. The microanatomy of the spleen makes new generation drugs such as monoclonal antibodies, nanoparticles, and liposomes accessible to the splenic parenchyma (Cataldi *et al.*, 2017). In the review of this information, our findings were compatible with the previous results. Additionally, we could not observe DNA origami penetration to brain parenchyma, which is expected for many compounds, not only nanoparticles, due to the blood-brain- barrier. Instead, the DNA origami signal was observable in the meningeal vessels and skull bone marrow, which have the relatively more permeable anatomy than the central nervous system. Along with this, DNA origami had a logical and expected whole-body distribution.

In order to test targeting of DNA origami *in vivo*, we conjugated it to a CX3CR1 antibody. This immune-targeting origami did not seem to change the distribution at first glance. However, in a closer look, mainly the liver and the spleen were targeted. The sinusoidal organization of CX3CR1 targeting origami was evidence by co-localization with Kupffer cells, which are the CX3CR1+ resident macrophages of the liver (Freitas-Lopes *et al.*, 2017). Since Kupffer cells make up 80% to 90% of all the macrophages in the entire body, high signal intensity in the liver supported the targeting efficiency of origami. In the spleen, immune-targeting origami primarily accumulated in the red pulp. The red pulp acts as a large reservoir for monocytes. These cells also bear CX3CR1. The population of monocytes in this reservoir is greater than the total number of monocytes present in circulation (den Haan and Kraal, 2012). The excessive signal in the spleen could be due to the targeting of these monocytes. In addition to the liver and spleen, lymph nodes, lungs, and thymus had immune-targeting DNA origami signals. Because the lungs are the first line of defense in the blood-air interface, they also consist of tissue macrophages. However, the lung signal was only detectable in higher magnifications because of their low number compared to the liver and spleen. The signal in these tissues is plausible because the lymph node and thymus are immune organs.

This signal observation could be fallacious to track DNA origami because of the tissue stability of DNA origami. If origami underwent degradation, the observed signal could come from free fluorophores. To test this phenomenon, we injected Atto647 and subjected the animal to the same procedure as the animals in other experimental groups. Even after 20 min of circulation, no signal was detectable in any of the organs. This suggests that Atto647 was not sustainable in the tissues and rapidly cleared from the body. Therefore, the signal detected in other groups should come

from intact origami because intact origami structures had longer *in vivo* signal retention. In case of breakdown, we have not been able to detect any signal in the tissues.

To further test the targeting efficiency, we injected DNA origami modalities into different animal models, i.e. cancer-targeting DNA origami to healthy and tumor-bearing animals. We also used the control groups, such as tumor-bearing animals with 6A10 cancer-targeting antibodies and non-targeting DNA origami injected. Cancer-targeting DNA origami successfully accumulated in metastatic tissues, mainly the lung and liver. We used 6A10 antibodies in the same concentration as the origami. The distribution of 6A10 seemed more random and dispersed than cancer-targeting origami. Especially liver had a surfeit antibody signal, which might cause toxic accumulation. A large amount of non-targeting origami accumulated in the spleen after one h circulation. As suggested before, this might be the result of time-dependent behavior. We observed cancer-targeting origami in the liver, where it could be metabolized down and cleared from the body in the healthy group when no cancer cells were present. Previously, we observed that DNA origami had a rapid tissue distribution. The conjugation of DNA origami with 6A10 antibody might increase the circulation time of DNA origami in the bloodstream. The half-life of antibodies in mice varies from 2 days to 8 days. In the former work, the therapeutic antibody circulated for two days before sacrifice, and the authors found that the antibody-targeted overall 77% of metastases. The low number of targeting in our research could be 1 hour of circulation time. To test this theory, we repeated the same experimental setup with longer circulation time (8 hours, 12 hours, and 24 hours, data not shown). However, we could not detect any origami signal after vDISCO for any extended circulation groups. Based on our clearance experiments, we can conclude that this is related to the stability of DNA origami within the body. Multiple injections of DNA origami or longer circulation time with higher stability of origami are required to increase the number of targeted metastases. The current effort focuses on the enhancement of *in vivo* stability.

DNA origami and DOX coupling provided enhanced passive tumor targeting and long-term properties, particularly with triangle-shaped DNA origami. In both *in vivo* and *in vitro*, DNA origami was highly effective at delivering doxorubicin into tumors (Zhang et al., 2014). In another research, DNA origami drug delivery vehicles improved the cellular uptake of doxorubicin, resulting in enhanced cell-killing activity against DOX-resistant MCF 7 cells (Jiang et al., 2012). Thus, we coupled cancer-targeting and non-targeting DNA origami with DOX. So far, we have explained the immune properties and targeting efficiency. The next step is the assessment of the cargo delivery potency. We took advantage of previously introduced DeepMACT unbiased AI-aided quantification technology to assess the anti-cancer effect of DOX in the presence or absence of DNA origami. Our data showed that the conjugation of the anti-cancer drug Doxorubicin with DNA origami could increase the targeting efficiency and decrease the adverse effect of the systemic distribution of DOX.

In previous reports, researchers used bioluminescence or fluorescent tomography to demonstrate the biodistribution of nanoparticles (Hahn *et al.*, 2014; Perrault and Shih, 2014b; Cuccarese *et al.*, 2017). At the whole-body mouse level, the resolution of these techniques is far from that needed for cell-level accuracy to evaluate precision. To prove the superiority of our technique, we used all the techniques mentioned, i.e. bioluminescence, fluorescent tomography, and tissue clearing. We not only observed the organ-wise distribution with vDISCO and LSFM, but also we were able to gather cell-level information. For instance, upon using higher magnification in LSFM, we identified Kupffer cell localization of immune-targeting origami in the liver. However, with bioluminescence and fluorescence tomography, only the organ-wise assumptions of the nanoparticles were possible. Furthermore, due to the short wavelength of many fluorophores or endogenous proteins, i.e. ATTO550 or eGFP, bioluminescence, and fluorescence tomography cannot detect them.

DNA origami has proven to be a versatile tool in the construction of various nanostructures; however, its limitations pose challenges in nanotechnology research. The primary limitation of DNA origami is the limited size and complexity of structures, which impedes the incorporation of multi-

ple functionalities within a single structure. Additionally, DNA origami structures are highly susceptible to environmental factors such as temperature, pH, and ionic strength, which can affect their stability. The cost and time involved in producing large quantities of DNA origami structures are still relatively high, which hinders their practical applications. Although we attempted to address these shortcomings in our study, further investigation is necessary to evaluate their significance. We plan to increase the number of subjects in future studies to obtain more in-depth results, especially for the quantification studies. In addition, the current study focused overall body detection of DNA origami; however, it lacks any molecular proof of DNA origami targeting efficiency. To provide molecular proof of DNA origami targeting efficiency, we will combine laser microdissection and proteomics. Additionally, as a functional cargo, we tried DOX conjugation with DNA origami, the efficiency of cargo delivery only assessed with fluorescent imaging and AI-based quantification. This experiment should be enhanced with increasing n number and molecular assessment of targeted and untargeted cancer cells to be able to evaluate cargo delivery evaluation. These efforts will help overcome the current limitations and improve the practical applications of DNA origami in nanotechnology research.

In our second attempt at functional cargo delivery, we aimed to target the atherosclerotic lesion sites, particularly the large arterial walls, using TMP195. However, regardless of the disease stage, DNA origami showed poor delivery into the lesions. While CX3CR1-positive atherosclerotic plaques were detected, immune-cell-targeting DNA origami signal was notably absent in most lesion areas, with limited penetration observed in only one zone of the mitral valve with atherosclerotic lesions. Furthermore, goat anti-CX3CR1-conjugated origami signal was detected in the liver and spleen of the same animals, overlapping with CX3CR1-positive cells. These results indicate that while DNA origami targeting and stability remained comparable to previous experiments, the penetration rate into atherosclerotic lesion areas was poor. The complex structure of atherosclerotic lesions, rich in immune cells, foam cells, and calcified zones, likely contributed to this poor penetration rate. Enhancing DNA nanoparticles' penetration into atherosclerotic arterial walls will require further efforts. One potential approach could involve combining DNA origami with lipid nanoparticles, leveraging the similarity of nanoparticle surface to lipids, cholesterol, and LDLs abundant in atherosclerotic lesions. However, due to the lack of successful penetration despite multiple attempts, we did not proceed further with functional cargo delivery. Conjugating TMP195 would likely increase the size of DNA nanoparticles, further hindering penetration.

In the future, new approaches will combine multi-omics studies with DNA origami research to provide more specific and customized treatment options by targeting cells based on their molecular signatures. Furthermore, thanks to DNA origami's upscale cargo capacity and programmability, multiple functional molecules can be combined with targeted DNA origami. To exemplify, drugs and inhibitors can be coupled for delivery, and fluorophores can be conjugated to monitor *in vivo* efficiency of these complex particles. All of these new technologies together will broaden the application horizons of nanoparticles *in vivo*.

In conclusion, we present the first methodological approach to developing nanocarriers controllable at the cellular level. We tested our pipeline with DNA-based nanoparticles, which can be applied to any nanoparticle in principle. It may prove helpful for developing tailored treatments in future studies, such as cancer metastasis treatment and somatic gene editing of user-specified cells.

4.1 Research Summary

Targeting nanoparticle therapeutics with cellular accuracy in whole organisms is a breakthrough opportunity for precision medicine. However, evaluating and fine-tuning biodistribution in the entire organism at the cellular level remains a significant obstacle. Here, we constructed nanoparticle drug mimetics based on DNA origami, a candidate drug delivery framework, and analyzed their biodistribution with single-cell accuracy in transparent mice using DISCO tissue clearing and whole-body light-sheet microscopy, in addition to studying tolerability, clearance kinetics, and immune response parameters. Untargeted DNA origami primarily accumulated in spleen and liver, while an immune cell-targeting nanoparticle variant successfully attached to immune cells throughout the whole mouse body. A cancer-targeting drug mimetic co-localized on solid-tumor metastasis in the liver and the lung. These findings indicate that DNA origami nanoparticles can be directed to and taken up by target cells *in vivo*, providing an important proof-of-concept that paves the way for precision medicine uses. It also highlights the potential of high-resolution tissue-clearing imaging technologies to support their development.

5. Publications

5.1 Single-cell precision DNA nanotechnology *in vivo*

DOI: https://doi.org/10.1101/2023.07.24.550304

Muge Molbay, Benjamin Kick, Shan Zhao, Mihail Ivilinov Todorov, Tzu-Lun Ohn, Stefan Roth, Alba Simats, Vikramjeet Singh, Igor Khalin, Chenchen Pan, Harsharan Singh Bhatia, Farida Hellal, Reinhard Zeidler, Arthur Liesz, Nikolaus Plesnila, Hendrik Dietz, Ali Erturk

5.2 A guidebook for DISCO tissue clearing

DOI: https://doi.org/10.15252/msb.20209807

Muge Molbay, Zeynep Ilgın Kolabaş and Ali Ertürk

5.3 Multi-omics and 3D-imaging reveal bone heterogeneity and unique calvaria cells in neuroinflammation

DOI: https://doi.org/10.1101/2021.12.24.473988

Zeynep Ilgin Kolabas, Louis B. Kuemmerle, Robert Perneczky, Benjamin Förstera, Maren Büttner , Ozum Sehnaz Caliskan, Mayar Ali, Zhouyi Rong, Hongcheng Mai , Selina Hummel, Laura M. Bartos, Gloria Biechele, Artem Zatcepin, Natalie L. Albert , Marcus Unterrainer, Johannes Gnörich, Shan Zhao, Igor Khalin , Boris-Stephan Rauchmann, **Muge Molbay**, Michael Sterr, Ines Kunze, Karen Stanic, Simon Besson-Girard, Anna Kopczak , Sabrina Katzdobler, Carla Palleis, Ozgun Gokce, Heiko Lickert, Hanno Steinke, Ingo Bechmann, Katharina Buerger, Johannes Levin, Christian Haass, Martin Dichgans, Joachim Havla, Tania Kümpfel, Martin Kerschensteiner, Mikael Simons, Nikolaus Plesnila, Natalie Krahmer, Harsharan Singh Bhatia, Suheda Erener, Farida Hellal, Matthias Brendel, Fabian J. Theis and Ali Erturk

5.4 Proteomics of spatially identified tissues in whole organs

DOI: https://doi.org/10.1016/j.cell.2022.11.021

Harsharan Singh Bhatia, Andreas-David Brunner, Zhouyi Rong, Hongcheng Mai, Marvin Thielert, Rami Al-Maskari, Johannes Christian Paetzold, Florian Kofler, Mihail Ivilinov Todorov, Mayar Ali, **Muge Molbay**, Zeynep Ilgin Kolabas, Doris Kaltenecker, Stephan Müller, Stefan F. Lichtenthaler, Bjoern H. Menze, Fabian J. Theis, Matthias Mann, Ali Ertürk

5.5 Whole-body nanobody labelling, clearing and imaging with vDISCO

DOI: https://doi.org/10.1038/s41596-022-00788-2

Ruiyao Cai[1,2], Zeynep Ilgin Kolabas[1,2,3], Doris Kaltenecker[1,2], Chenchen Pan[1,2], Hongcheng Mai[1,2], Shan Zhao[1,2], **Muge Molbay**[1,2,4] Tzu-Lun Ohn[1,2,] and Ali Ertürk[1,2,5]

References

Alexis, F. *et al.* (2008) 'Factors Affecting the Clearance and Biodistribution of Polymeric Nano-particles', *Molecular Pharmaceutics*, 5(4), pp. 505–515. Available at: https://doi.org/10.1021/mp800051m.

Angell, C. *et al.* (2016) 'DNA Nanotechnology for Precise Control over Drug Delivery and Gene Therapy', *Small (Weinheim an Der Bergstrasse, Germany)*, 12(9), pp. 1117–1132. Available at: https://doi.org/10.1002/smll.201502167.

Apostolakis, S. *et al.* (2007) 'Effects of polymorphisms in chemokine ligands and receptors on susceptibility to coronary artery disease', *Thrombosis Research*, 119(1), pp. 63–71. Available at: https://doi.org/10.1016/j.thromres.2005.12.016.

Arora, A.A. and de Silva, C. (2018) 'Beyond the smiley face: applications of structural DNA nan-otechnology', *Nano Reviews & Experiments*, 9(1), p. 1430976. Available at: https://doi.org/10.1080/20022727.2018.1430976.

Benson, E. *et al.* (2015) 'DNA rendering of polyhedral meshes at the nanoscale', *Nature*, 523(7561), pp. 441–444. Available at: https://doi.org/10.1038/nature14586.

Bjerkeli, V. *et al.* (2007) 'Increased expression of fractalkine (CX3CL1) and its receptor, CX3CR1, in Wegener's granulomatosis--possible role in vascular inflammation', *Rheumatology (Oxford, England)*, 46(9), pp. 1422–1427. Available at: https://doi.org/10.1093/rheumatol-ogy/kem168.

Bray, F. *et al.* (2018) 'Global cancer statistics 2018: GLOBOCAN estimates of incidence and mortality worldwide for 36 cancers in 185 countries', *CA: a cancer journal for clinicians*, 68(6), pp. 394–424. Available at: https://doi.org/10.3322/caac.21492.

Bria, A. and Iannello, G. (2012) 'TeraStitcher - A tool for fast automatic 3D-stitching of teravoxel-sized microscopy images', *BMC Bioinformatics*, 13(1), p. 316. Available at: https://doi.org/10.1186/1471-2105-13-316.

Bursill, C.A., Channon, K.M. and Greaves, D.R. (2004) 'The role of chemokines in atherosclero-sis: recent evidence from experimental models and population genetics', *Current Opinion in Lip-idology*, 15(2), pp. 145–149. Available at: https://doi.org/10.1097/00041433-200404000-00007.

Cai, R. *et al.* (2019) 'Panoptic imaging of transparent mice reveals whole-body neuronal projec-tions and skull-meninges connections', *Nature Neuroscience*, 22(2), pp. 317–327. Available at: https://doi.org/10.1038/s41593-018-0301-3.

Cataldi, M. *et al.* (2017) 'Emerging Role of the Spleen in the Pharmacokinetics of Monoclonal Antibodies, Nanoparticles and Exosomes', *International Journal of Molecular Sciences*, 18(6), p. 1249. Available at: https://doi.org/10.3390/ijms18061249.

Chandrasekaran, A.R. *et al.* (2016) 'Beyond the Fold: Emerging Biological Applications of DNA Origami', *Chembiochem: A European Journal of Chemical Biology*, 17(12), pp. 1081–1089. Available at: https://doi.org/10.1002/cbic.201600038.

Chandrasekaran, A.R. (2016) 'Designer DNA Architectures: Applications in Nanomedicine', *Nanobiomedicine*, 3, p. 6. Available at: https://doi.org/10.5772/63228.

Chandrasekaran, A.R. *et al.* (2017) 'Addressable configurations of DNA nanostructures for re-writable memory', *Nucleic Acids Research*, 45(19), pp. 11459–11465. Available at: https://doi.org/10.1093/nar/gkx777.

Chandrasekaran, A.R. *et al.* (2018) *Detection of cellular microRNAs with programmable DNA nanoswitches*. preprint. Bioengineering. Available at: https://doi.org/10.1101/334631.

Chandrasekaran, A.R. (2018) 'Reconfigurable DNA Nanoswitches for Graphical Readout of Molecular Signals', *ChemBioChem*, 19(10), pp. 1018–1021. Available at: https://doi.org/10.1002/cbic.201800057.

Chen, Z., Ross, J.L. and Hambardzumyan, D. (2019) 'Intravital 2-photon imaging reveals distinct morphology and infiltrative properties of glioblastoma-associated macrophages', *Proceedings of the National Academy of Sciences*, 116(28), pp. 14254–14259. Available at: https://doi.org/10.1073/pnas.1902366116.

Chung, K. *et al.* (2013) 'Structural and molecular interrogation of intact biological systems', *Nature*, 497(7449), pp. 332–337. Available at: https://doi.org/10.1038/nature12107.

Combadière, C. *et al.* (2003) 'Decreased atherosclerotic lesion formation in CX3CR1/apolipo-protein E double knockout mice', *Circulation*, 107(7), pp. 1009–1016. Available at: https://doi.org/10.1161/01.cir.0000057548.68243.42.

Cuccarese, M.F. *et al.* (2017) 'Heterogeneity of macrophage infiltration and therapeutic response in lung carcinoma revealed by 3D organ imaging', *Nature Communications*, 8(1), p. 14293. Available at: https://doi.org/10.1038/ncomms14293.

Cybulsky, M.I. and Hegele, R.A. (2003) 'The fractalkine receptor CX3CR1 is a key mediator of atherogenesis', *Journal of Clinical Investigation*, 111(8), pp. 1118–1120. Available at: https://doi.org/10.1172/JCI200318237.

Dent, J.A., Polson, A.G. and Klymkowsky, M.W. (1989) 'A whole-mount immunocytochemical analysis of the expression of the intermediate filament protein vimentin in Xenopus', *Development*, 105(1), pp. 61–74.

Douglas, S.M. *et al.* (2009) 'Self-assembly of DNA into nanoscale three-dimensional shapes', *Nature*, 459(7245), pp. 414–418. Available at: https://doi.org/10.1038/nature08016.

Endo, M. *et al.* (2010a) 'A versatile DNA nanochip for direct analysis of DNA base-excision repair', *Angewandte Chemie (International Ed. in English)*, 49(49), pp. 9412–9416. Available at: https://doi.org/10.1002/anie.201003604.

Endo, M. *et al.* (2010b) 'A Versatile DNA Nanochip for Direct Analysis of DNA Base-Excision Repair', *Angewandte Chemie International Edition*, 49(49), pp. 9412–9416. Available at: https://doi.org/10.1002/anie.201003604.

Engelhardt, F.A.S. *et al.* (2019) 'Custom-Size, Functional, and Durable DNA Origami with Design-Specific Scaffolds', *ACS nano*, 13(5), pp. 5015–5027. Available at: https://doi.org/10.1021/acsnano.9b01025.

Ertürk, A. *et al.* (2012) 'Three-dimensional imaging of solvent-cleared organs using 3DISCO', *Nature Protocols*, 7(11), pp. 1983–1995. Available at: https://doi.org/10.1038/nprot.2012.119.

Freitas-Lopes, M.A. *et al.* (2017) 'Differential Location and Distribution of Hepatic Immune Cells', *Cells*, 6(4), p. 48. Available at: https://doi.org/10.3390/cells6040048.

Gradinaru, V. *et al.* (2018) 'Hydrogel-Tissue Chemistry: Principles and Applications', *Annual review of biophysics*, 47, pp. 355–376. Available at: https://doi.org/10.1146/annurev-biophys-070317-032905.

Greenbaum, A. *et al.* (2017) 'Bone CLARITY: Clearing, imaging, and computational analysis of osteoprogenitors within intact bone marrow', *Science Translational Medicine*, 9(387). Available at: https://doi.org/10.1126/scitranslmed.aah6518.

Guengerich, F.P. (2011) 'Mechanisms of Drug Toxicity and Relevance to Pharmaceutical Development', *Drug metabolism and pharmacokinetics*, 26(1), pp. 3–14.

den Haan, J.M.M. and Kraal, G. (2012) 'Innate Immune Functions of Macrophage Subpopulations in the Spleen', *Journal of Innate Immunity*, 4(5–6), pp. 437–445. Available at: https://doi.org/10.1159/000335216.

Hahn, J. *et al.* (2014) 'Addressing the Instability of DNA Nanostructures in Tissue Culture', *ACS Nano*, 8(9), pp. 8765–8775. Available at: https://doi.org/10.1021/nn503513p.

Hama, H. *et al.* (2011) 'Scale: a chemical approach for fluorescence imaging and reconstruction of transparent mouse brain', *Nature Neuroscience*, 14(11), pp. 1481–1488. Available at: https://doi.org/10.1038/nn.2928.

Hama, H. *et al.* (2015) 'ScaleS: an optical clearing palette for biological imaging', *Nature Neuroscience*, 18(10), pp. 1518–1529. Available at: https://doi.org/10.1038/nn.4107.

Hansson, G.K. (2005) 'Inflammation, atherosclerosis, and coronary artery disease', *The New England Journal of Medicine*, 352(16), pp. 1685–1695. Available at: https://doi.org/10.1056/NEJMra043430.

von Holt, K. *et al.* (2009) 'Progression of atherosclerosis in the Apo E-/- model: 12-month exposure to cigarette mainstream smoke combined with high-cholesterol/fat diet', *Atherosclerosis*, 205(1), pp. 135–143. Available at: https://doi.org/10.1016/j.atherosclerosis.2008.11.031.

Hong, F. *et al.* (2017) 'DNA Origami: Scaffolds for Creating Higher Order Structures', *Chemical Reviews*, 117(20), pp. 12584–12640. Available at: https://doi.org/10.1021/acs.chemrev.6b00825.

Jiang, D. *et al.* (2018) 'DNA origami nanostructures can exhibit preferential renal uptake and alleviate acute kidney injury', *Nature Biomedical Engineering*, 2(11), pp. 865–877. Available at: https://doi.org/10.1038/s41551-018-0317-8.

Jones, M.R., Seeman, N.C. and Mirkin, C.A. (2015) 'Programmable materials and the nature of the DNA bond', *Science* [Preprint]. Available at: https://www.science.org/doi/abs/10.1126/science.1260901 (Accessed: 4 January 2022).

Jun, H., Shepherd, T.R., *et al.* (2019) 'Automated Sequence Design of 3D Polyhedral Wireframe DNA Origami with Honeycomb Edges', *ACS Nano*, 13(2), pp. 2083–2093. Available at: https://doi.org/10.1021/acsnano.8b08671.

Jun, H., Zhang, F., *et al.* (2019) 'Autonomously designed free-form 2D DNA origami', *Science Advances* [Preprint]. Available at: https://doi.org/10.1126/sciadv.aav0655.

Ke, M.-T., Fujimoto, S. and Imai, T. (2013) 'SeeDB: a simple and morphology-preserving optical clearing agent for neuronal circuit reconstruction', *Nature Neuroscience*, 16(8), pp. 1154–1161. Available at: https://doi.org/10.1038/nn.3447.

Khalin, I. *et al.* (2020) 'Ultrabright Fluorescent Polymeric Nanoparticles with a Stealth Pluronic Shell for Live Tracking in the Mouse Brain', *ACS Nano* [Preprint]. Available at: https://doi.org/10.1021/acsnano.0c01505.

Kim, K.-R. *et al.* (2013) 'Sentinel lymph node imaging by a fluorescently labeled DNA tetrahedron', *Biomaterials*, 34(21), pp. 5226–5235. Available at: https://doi.org/10.1016/j.biomaterials.2013.03.074.

Kim, K.-R. *et al.* (2016) 'Self-assembled mirror DNA nanostructures for tumor-specific delivery of anticancer drugs', *Journal of Controlled Release: Official Journal of the Controlled Release Society*, 243, pp. 121–131. Available at: https://doi.org/10.1016/j.jconrel.2016.10.015.

Kim, K.-R. *et al.* (2020) 'A self-assembled DNA tetrahedron as a carrier for in vivo liver-specific delivery of siRNA', *Biomaterials Science*, 8(2), pp. 586–590. Available at: https://doi.org/10.1039/C9BM01769K.

Kiviaho, J.K. *et al.* (2016) 'Cationic polymers for DNA origami coating – examining their binding efficiency and tuning the enzymatic reaction rates', *Nanoscale*, 8(22), pp. 11674–11680. Available at: https://doi.org/10.1039/C5NR08355A.

Klymkowsky, M.W. and Hanken, J. (1991) 'Chapter 22 Whole-Mount Staining of Xenopus and Other Vertebrates', in *Methods in Cell Biology*. Elsevier, pp. 419–441. Available at: https://doi.org/10.1016/S0091-679X(08)60290-3.

Krieg, A.M. (2002) 'CpG motifs in bacterial DNA and their immune effects', *Annual Review of Immunology*, 20, pp. 709–760. Available at: https://doi.org/10.1146/annurev.immunol.20.100301.064842.

Lee, M. *et al.* (2018) 'Tissue-specific Role of CX3CR1 Expressing Immune Cells and Their Relationships with Human Disease', *Immune Network*, 18(1), p. e5. Available at: https://doi.org/10.4110/in.2018.18.e5.

Lesnik, P., Haskell, C.A. and Charo, I.F. (2003) 'Decreased atherosclerosis in CX3CR1–/– mice reveals a role for fractalkine in atherogenesis', *Journal of Clinical Investigation*, 111(3), pp. 333–340. Available at: https://doi.org/10.1172/JCI200315555.

Linton, M.F. *et al.* (2000) 'The Role of Lipids and Lipoproteins in Atherosclerosis', in K.R. Feingold et al. (eds) *Endotext*. South Dartmouth (MA): MDText.com, Inc. Available at: http://www.ncbi.nlm.nih.gov/books/NBK343489/ (Accessed: 24 March 2023).

Lo Sasso, G. *et al.* (2016) 'The Apoe−/− mouse model: a suitable model to study cardiovascular and respiratory diseases in the context of cigarette smoke exposure and harm reduction', *Journal of Translational Medicine*, 14, p. 146. Available at: https://doi.org/10.1186/s12967-016-0901-1.

Lucas, C.R. *et al.* (2022) 'DNA Origami Nanostructures Elicit Dose-Dependent Immunogenicity and Are Nontoxic up to High Doses In Vivo', *Small*, 18(26), p. 2108063. Available at: https://doi.org/10.1002/smll.202108063.

Malyala, P. and Singh, M. (2008) 'Endotoxin limits in formulations for preclinical research', *Journal of Pharmaceutical Sciences*, 97(6), pp. 2041–2044. Available at: https://doi.org/10.1002/jps.21152.

Masimirembwa, C.M., Bredberg, U. and Andersson, T.B. (2003) 'Metabolic Stability for Drug Discovery and Development', *Clinical Pharmacokinetics*, 42(6), pp. 515–528. Available at: https://doi.org/10.2165/00003088-200342060-00002.

Mathur, D. and Medintz, I.L. (2019) 'The Growing Development of DNA Nanostructures for Potential Healthcare-Related Applications', *Advanced Healthcare Materials*, 8(9), p. e1801546. Available at: https://doi.org/10.1002/adhm.201801546.

McDermott, D.H. *et al.* (2003) 'Chemokine receptor mutant CX3CR1-M280 has impaired adhesive function and correlates with protection from cardiovascular disease in humans', *Journal of Clinical Investigation*, 111(8), pp. 1241–1250. Available at: https://doi.org/10.1172/JCI200316790.

Messaoudi, S., Greschner, A.A. and Gauthier, M.A. (2019) 'Progress Toward Absorption, Distribution, Metabolism, Elimination, and Toxicity of DNA Nanostructures', *Advanced Therapeutics*, 2(12), p. 1900144. Available at: https://doi.org/10.1002/adtp.201900144.

Mirshafiee, V. *et al.* (2013) 'Protein corona significantly reduces active targeting yield', *Chemical Communications*, 49(25), pp. 2557–2559. Available at: https://doi.org/10.1039/C3CC37307J.

Molbay, M. *et al.* (2021) 'A guidebook for DISCO tissue clearing', *Molecular Systems Biology*, 17(3), p. e9807. Available at: https://doi.org/10.15252/msb.20209807.

Muller, P.Y. and Milton, M.N. (2012) 'The determination and interpretation of the therapeutic index in drug development', *Nature Reviews Drug Discovery*, 11(10), pp. 751–761. Available at: https://doi.org/10.1038/nrd3801.

Nickels, P.C. *et al.* (2014) 'DNA origami structures directly assembled from intact bacteriophages', *Small (Weinheim an Der Bergstrasse, Germany)*, 10(9), pp. 1765–1769. Available at: https://doi.org/10.1002/smll.201303442.

Nus, M. and Mallat, Z. (2016) 'Immune-mediated mechanisms of atherosclerosis and implications for the clinic', *Expert Review of Clinical Immunology*, 12(11), pp. 1217–1237. Available at: https://doi.org/10.1080/1744666X.2016.1195686.

Oh, J.Y. *et al.* (2018) 'Cloaking nanoparticles with protein corona shield for targeted drug delivery', *Nature Communications*, 9(1), p. 4548. Available at: https://doi.org/10.1038/s41467-018-06979-4.

Pan, C. *et al.* (2016) 'Shrinkage-mediated imaging of entire organs and organisms using uDISCO', *Nature Methods*, 13(10), pp. 859–867. Available at: https://doi.org/10.1038/nmeth.3964.

Pan, C. *et al.* (2019a) 'Deep learning reveals cancer metastasis and therapeutic antibody targeting in the entire body', *Cell*, 179(7), pp. 1661-1676.e19. Available at: https://doi.org/10.1016/j.cell.2019.11.013.

Pan, C. *et al.* (2019b) 'Deep Learning Reveals Cancer Metastasis and Therapeutic Antibody Targeting in the Entire Body', *Cell*, 179(7), pp. 1661-1676.e19. Available at: https://doi.org/10.1016/j.cell.2019.11.013.

Park, Y.-G. *et al.* (2019) 'Protection of tissue physicochemical properties using polyfunctional crosslinkers', *Nature Biotechnology*, 37(1), pp. 73–83. Available at: https://doi.org/10.1038/nbt.4281.

Perrault, S.D. and Shih, W.M. (2014a) 'Virus-inspired membrane encapsulation of DNA nanostructures to achieve in vivo stability', *ACS nano*, 8(5), pp. 5132–5140. Available at: https://doi.org/10.1021/nn5011914.

Perrault, S.D. and Shih, W.M. (2014b) 'Virus-Inspired Membrane Encapsulation of DNA Nanostructures To Achieve In Vivo Stability', *ACS Nano*, 8(5), pp. 5132–5140. Available at: https://doi.org/10.1021/nn5011914.

Piskunen, P. *et al.* (2020) 'Increasing Complexity in Wireframe DNA Nanostructures', *Molecules*, 25(8), p. 1823. Available at: https://doi.org/10.3390/molecules25081823.

Ponnuswamy, N. *et al.* (2017) 'Oligolysine-based coating protects DNA nanostructures from low-salt denaturation and nuclease degradation', *Nature Communications*, 8(1), p. 15654. Available at: https://doi.org/10.1038/ncomms15654.

Praetorius, F. *et al.* (2017) 'Biotechnological mass production of DNA origami', *Nature*, 552(7683), pp. 84–87. Available at: https://doi.org/10.1038/nature24650.

Renier, N. *et al.* (2016) 'Mapping of Brain Activity by Automated Volume Analysis of Immediate Early Genes', *Cell*, 165(7), pp. 1789–1802. Available at: https://doi.org/10.1016/j.cell.2016.05.007.

Rothemund, P.W.K. (2006) 'Folding DNA to create nanoscale shapes and patterns', *Nature*, 440(7082), pp. 297–302. Available at: https://doi.org/10.1038/nature04586.

Santi, M. *et al.* (2017) 'Rational Design of a Transferrin-Binding Peptide Sequence Tailored to Targeted Nanoparticle Internalization', *Bioconjugate Chemistry*, 28(2), pp. 471–480. Available at: https://doi.org/10.1021/acs.bioconjchem.6b00611.

Seeman, N.C. (1982) 'Nucleic acid junctions and lattices', *Journal of Theoretical Biology*, 99(2), pp. 237–247. Available at: https://doi.org/10.1016/0022-5193(82)90002-9.

Setyawati, M.I., Kutty, R.V. and Leong, D.T. (2016) 'DNA Nanostructures Carrying Stoichiometrically Definable Antibodies', *Small (Weinheim an Der Bergstrasse, Germany)*, 12(40), pp. 5601–5611. Available at: https://doi.org/10.1002/smll.201601669.

Silvestri, L. *et al.* (2016) 'Clearing of fixed tissue: a review from a microscopist's perspective', *Journal of Biomedical Optics*, 21(8), p. 081205. Available at: https://doi.org/10.1117/1.JBO.21.8.081205.

Singh, R.B. *et al.* (2002) 'Pathogenesis of atherosclerosis: A multifactorial process', *Experimental & Clinical Cardiology*, 7(1), pp. 40–53.

Spalteholz, W. (1914) *Über das Durchsichtigmachen von menschlichen und tierischen Präparaten und seine theoretischen Bedingungen, nebst Anhang: Über Knochenfärbung.* Leipzig: S. Hirzel.

Stahl, E. *et al.* (2014) 'Facile and Scalable Preparation of Pure and Dense DNA Origami Solutions', *Angewandte Chemie International Edition*, 53(47), pp. 12735–12740. Available at: https://doi.org/10.1002/anie.201405991.

Sun, W. *et al.* (2014) 'Casting inorganic structures with DNA molds', *Science (New York, N.Y.)*, 346(6210), p. 1258361. Available at: https://doi.org/10.1126/science.1258361.

Surana, S., Bhatia, D. and Krishnan, Y. (2013) 'A method to study in vivo stability of DNA nanostructures', *Methods (San Diego, Calif.)*, 64(1), pp. 94–100. Available at: https://doi.org/10.1016/j.ymeth.2013.04.002.

Surana, S., Shenoy, A.R. and Krishnan, Y. (2015) 'Designing DNA nanodevices for compatibility with the immune system of higher organisms', *Nature Nanotechnology*, 10(9), pp. 741–747. Available at: https://doi.org/10.1038/nnano.2015.180.

Tainaka, K. *et al.* (2014) 'Whole-Body Imaging with Single-Cell Resolution by Tissue Decolorization', *Cell*, 159(4), pp. 911–924. Available at: https://doi.org/10.1016/j.cell.2014.10.034.

Teupser, D. *et al.* (2004) 'Major reduction of atherosclerosis in fractalkine (CX3CL1)-deficient mice is at the brachiocephalic artery, not the aortic root', *Proceedings of the National Academy of Sciences of the United States of America*, 101(51), pp. 17795–17800. Available at: https://doi.org/10.1073/pnas.0408096101.

Tian, C. *et al.* (2017) 'DNA Nanostructures-Mediated Molecular Imprinting Lithography', *ACS Nano*, 11(1), pp. 227–238. Available at: https://doi.org/10.1021/acsnano.6b04777.

Tulenko, T.N. and Sumner, A.E. (2002) 'The physiology of lipoproteins', *Journal of Nuclear Cardiology: Official Publication of the American Society of Nuclear Cardiology*, 9(6), pp. 638–649. Available at: https://doi.org/10.1067/mnc.2002.128959.

Tuttolomondo, A. *et al.* (2012) 'Arterial stiffness and ischemic stroke in subjects with and without metabolic syndrome', *Atherosclerosis*, 225(1), pp. 216–219. Available at: https://doi.org/10.1016/j.atherosclerosis.2012.08.027.

Wang, B. *et al.* (2013) 'Metabolism of Nanomaterials in Vivo: Blood Circulation and Organ Clearance', *Accounts of Chemical Research*, 46(3), pp. 761–769. Available at: https://doi.org/10.1021/ar2003336.

Wu, C. *et al.* (2013) 'Building a Multifunctional Aptamer-Based DNA Nanoassembly for Targeted Cancer Therapy', *Journal of the American Chemical Society*, 135(49), pp. 18644–18650. Available at: https://doi.org/10.1021/ja4094617.

Xavier, P.L. and Chandrasekaran, A.R. (2018) 'DNA-based construction at the nanoscale: emerging trends and applications', *Nanotechnology*, 29(6), p. 062001. Available at: https://doi.org/10.1088/1361-6528/aaa120.

Yanisch-Perron, C., Vieira, J. and Messing, J. (1985) 'Improved M13 phage cloning vectors and host strains: nucleotide sequences of the M13mp18 and pUC19 vectors', *Gene*, 33(1), pp. 103–119. Available at: https://doi.org/10.1016/0378-1119(85)90120-9.

Zhang, Q. *et al.* (2014) 'DNA Origami as an In Vivo Drug Delivery Vehicle for Cancer Therapy', *ACS Nano*, 8(7), pp. 6633–6643. Available at: https://doi.org/10.1021/nn502058j.

Zhang, S.H. *et al.* (1992) 'Spontaneous hypercholesterolemia and arterial lesions in mice lacking apolipoprotein E', *Science (New York, N.Y.)*, 258(5081), pp. 468–471. Available at: https://doi.org/10.1126/science.1411543.

Acknowledgements

Words cannot express my gratitude to my scientific supervisor Prof. Ali Ertürk and my mentor Dr. Farida Hellal for their invaluable patience and feedback. I also could not have undertaken this journey without my thesis supervisor Prof. Dr. Nikolaus Plesnila and Prof. Dr. Arthur Liesz, one of my thesis advisory committee members, who generously provided knowledge and expertise. Additionally, this endeavor would not have been possible without the generous support from the Turkish Ministry of Education, who financed my PhD.

I am also grateful to my colleagues, within and out of the lab, for their editing help, late-night feedback sessions, and moral support.

With a special mention to the Institute of Stroke and Dementia, where provided me an open, free, comfortable and scientific working environment and gave access to the laboratory, research facilities and animal facilities. Without the whole precious and systematic supports it would not be possible to conduct this research. To my enrolling Munich Medical Research School (MMRS), it was fantastic to have the opportunity to conduct my PhD under its great organization.

A very special gratitude goes out to all friends. Dr. Oguz Top, Edanur Ates Öz, Yasin Öz, Dr. Gökhan Dede, Esra Kagitci Dede, Dr. Ilgin Kolabas, Dr. Ceren Kimna, Denise Jeridi, Dr. Safiah Olabi and many others that provided me a great moral and emotional support through the though times.

Lastly, I would be remiss in not mentioning my family, for giving birth to me, raised me and supported me whole through my life. Their belief in me has kept my spirits and motivation high during this process. I would also like to thank to Rifki who gave me love, hope and strength during the challenging times.

LUDWIG-
MAXIMILIANS-
UNIVERSITÄT
MÜNCHEN

Dean's Office Medical Faculty
Faculty of Medicine

Affidavit

Molbay, Müge

Surname, first name

Address

I hereby declare, that the submitted thesis entitled

"Designing and Monitoring DNA Origami Particles for Single-Cell Precision Delivery"

is my own work. I have only used the sources indicated and have not made unauthorised use of services of a third party. Where the work of others has been quoted or reproduced, the source is always given.

I further declare that the dissertation presented here has not been submitted in the same or similar form to any other institution for the purpose of obtaining an academic degree.

Müge Molbay

München, 11.05.2023

Place, Date

Signature doctoral candidate

LMU | LUDWIG-
MAXIMILIANS-
UNIVERSITÄT
MÜNCHEN | Dean's Office Medical Faculty
Doctoral Office |

Confirmation of congruency between printed and electronic version of the doctoral thesis

Doctoral candidate: Müge Molbay

Address:

I hereby declare that the electronic version of the submitted thesis, entitled

"Designing and Monitoring DNA Origami Particles for Single-Cell Precision Delivery"

is congruent with the printed version both in content and format.

München, 11.05.2023

Place, Date

Müge Molbay

Signature doctoral candidate